THE SECOND WIND FORECAST IMPROVEMENT PROJECT (WFIP2)

Observational Field Campaign

James M. Wilczak, Mark Stoelinga, Larry K. Berg, Justin Sharp, Caroline Draxl, Katherine McCaffrey, Robert M. Banta, Laura Bianco, Irina Djalalova, Julie K. Lundquist, Paytsar Muradyan, Aditya Choukulkar, Laura Leo, Timothy Bonin, Yelena Pichugina, Richard Eckman, Charles N. Long, Kathleen Lantz, Rochelle P. Worsnop, Jim Bickford, Nicola Bodini, Duli Chand, Andrew Clifton, Joel Cline, David R. Cook, Harindra J. S. Fernando, Katja Friedrich, Raghavendra Krishnamurthy, Melinda Marquis, Jim McCaa, Joseph B. Olson, Sebastian Otarola-Bustos, George Scott, William J. Shaw, Sonia Wharton, and Allen B. White

The science of wind energy forecasting has taken a leap forward with the unique meteorological observations gathered in complex terrain during WFIP2.

Atmospheric flows in complex terrain play an important role in both the siting and the operation of many wind energy plants in the United States. First, wind plants, and even individual turbines, frequently are situated to exploit local accelerations of the flow due to the orography, with the goal of maximizing wind energy production. Second, the complexity of atmospheric flows in mountainous or hilly regions can make it more challenging to forecast how strong those winds will be and how much power will be produced at any given time. Importantly, accurate forecasts of wind power can reduce the cost of wind energy (Marquis et al. 2011) and accelerate its expansion. Third, strong low-level shears across the turbine rotor layer and increased turbulence intensity due to topography can reduce the life-span of wind turbines. For these reasons, improving our understanding of atmospheric flows in complex terrain, our ability to predict them, and their potential interaction with wind turbines are important for the advancement of wind energy.

The Columbia River Gorge and basin region is an exceptional natural observatory for studying meteorological phenomena associated with complex terrain. A near–sea level gap takes the Columbia River through the Cascade Range, a mountainous barrier 1,500–1,900 m high. The Cascades are scattered with high volcanic peaks (Mount Rainier: 4,392 m; Mount Adams: 3,473 m; and Mount Hood: 3,428 m) that tower above the near–sea level valleys to the east and west (Fig. 1). The canyon carved by the Columbia River continues eastward from the Cascade crest for over 50 km, and then opens into the vast Columbia River basin east of the Cascades. The Columbia River basin is surrounded by high terrain on all sides, and comprises much of eastern Washington and Oregon. The properties of the air sheds west and east of the Cascades are often radically different, yielding large

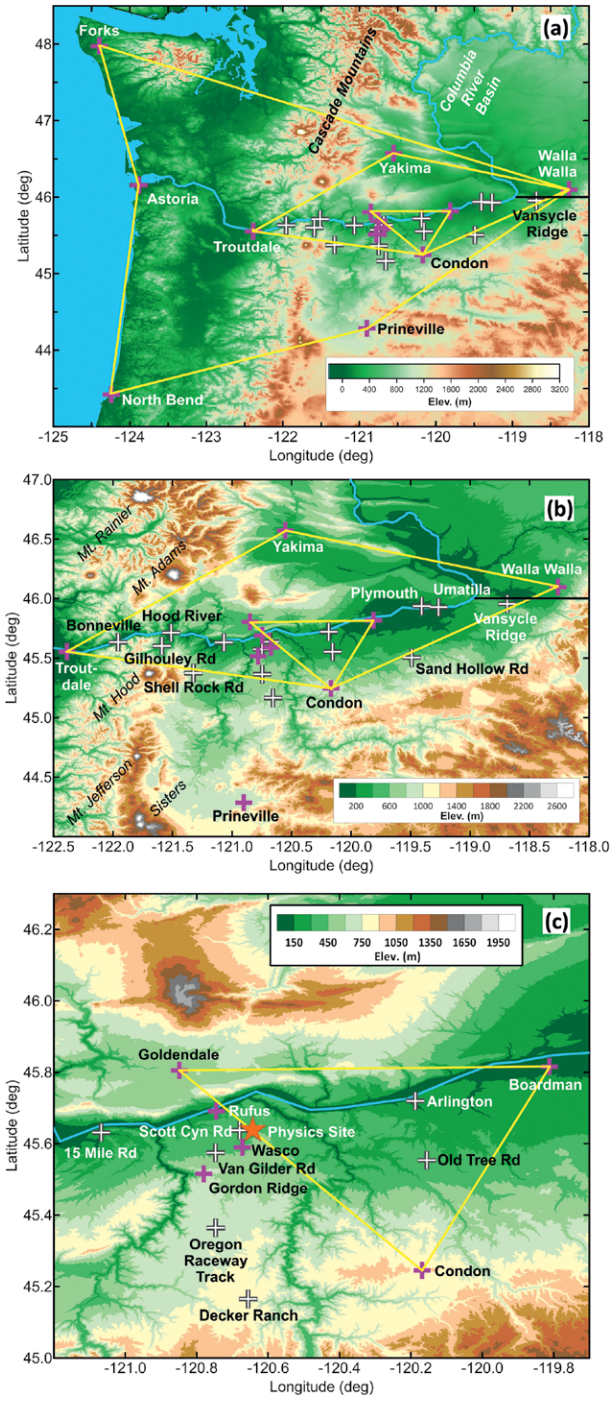

Fig. 1. Base maps showing all WFIP2 observation sites. Magenta crosses are "supersites," where several different types of complementary instruments were deployed, and white crosses are sites with simpler observing systems. (a) Yellow lines indicate the telescoping scales of observations. (b) Intermediate scale, with major mountain peaks indicated. (c) Finescale, with the location of the physics site indicated by the red star.

gradients in moisture, temperature, and pressure in the lower atmosphere. Air may be guided downslope and channeled, piled up in natural reservoirs, or forced up over more stable air below depending on atmospheric conditions. The results are cold pools, gap flows, mountain waves, mountain wakes, downslope flows, and mountain–valley circulations that occur on many different temporal and spatial scales. All of these vary in intensity and behavior depending on atmospheric conditions, and all present unique challenges to short-term forecasting for wind energy in the region. In addition to these complex meteorological phenomena, and in part because of them, the Columbia basin is also home to a large amount (more than 6 GW) of wind energy production. Because of this, the Columbia River basin in the Pacific Northwest was selected by the U.S. Department of Energy (DOE) as the study region for the Second Wind Forecast Improvement Project (WFIP2).

WFIP2 is a DOE- and National Oceanic and Atmospheric Administration (NOAA)-funded program that aims to improve the accuracy of NWP forecasts of wind speed in complex terrain for wind energy applications. Core components of WFIP2 included an 18-month (October 2015–March 2017) field campaign in the Columbia River Gorge and basin, an extensive numerical weather prediction (NWP) model development and evaluation effort, and the transfer of new knowledge gained from WFIP2 to support the decision-making process for routine operation of the electric grid. This article focuses on the WFIP2 observational field campaign, while companion articles in *BAMS* provide an overview of the entire project (Shaw et al. 2019), numerical model development (Olson et al. 2019), and the industry decision support mechanism (Grimit et al. 2019, manuscript submitted to *Bull. Amer. Meteor. Soc.*).

INSTRUMENTATION, DATA, AND PRODUCTS. Two central purposes of the WFIP2 instrumentation deployment were, first, to characterize the physical processes driving key meteorological phenomena in the area and, second, to critically evaluate and improve model physical parameterization schemes. Both of these tasks require simultaneous measurement of many different parameters to unravel the complex interactions occurring in the atmosphere and in model parameterizations, and to allow one to improve the parameterizations based on physical principles rather than ad hoc assumptions and tuning. To achieve these goals, a large and diverse set of remote sensing and in situ instruments were

assembled from DOE and NOAA national laboratories, Vaisala, universities, and industry partners.

The WFIP2 instruments were deployed in nested arrays of telescoping scales (Fig. 1a), with the outer scale documenting the synoptic/mesoscale setting and whether it was accurately depicted in the NWP models (indicated by the largest geometrical shape shown with yellow lines). Next, an intermediate scale quantified meteorological processes affecting boundary layer winds over a variety of terrain types, including locations both east and west of the Cascade Mountains (trapezoidal-shaped area, shown in more detail in Fig. 1b). Finally, an inner domain focused on a local region where there is a high concentration of wind plants [small triangular area, shown in detail in Fig. 1c; see also Fig. 1 in Shaw et al. (2019) for locations of wind plants]. The vertices of each of the telescoping geometrical shapes (yellow lines in Fig. 1) all had a radar wind profiler (RWP): the three sites along the Pacific coast had 449-MHz systems, typically providing winds up to 7–8 km and radio acoustic sounding system (RASS) temperatures to 1–2 km, while the other inland sites hosted 915-MHz systems providing winds to 3–4 km and RASS temperatures to 1 km. "Supersites" with several different types of complementary observing systems (including, for example, profiling Doppler sodars, scanning or profiling wind lidars, and profiling microwave radiometers) appear as magenta symbols. The remaining sites, with simpler observing systems typically comprising one or two instruments, are indicated by white symbols.

The long axis of the intermediate-scale trapezoid follows the course of the Columbia River (Fig. 1b). The Columbia River Gorge, located between Troutdale, Oregon, and Hood River, is the only major sea level pass through the Cascade Mountain Range, leading to intense gap flows through the gorge, while the tall volcanic peaks in the Cascade Range frequently generate mountain wakes. For the smaller triangular-shaped nest (Fig. 1c), the sites at 15 Mile Road, Rufus, Arlington, and Boardman, Oregon, form a transect

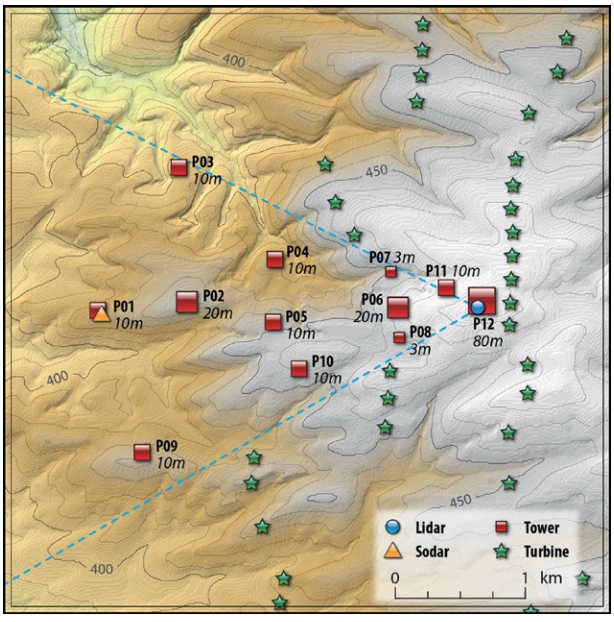

Fig. 2. Elevation base map of the physics site, with a terrain contour interval of 10 m. Green stars are wind turbine locations; red squares are instrumented towers (3–20 m tall); the yellow triangle is a mast, sodar, and surface energy budget site; and the blue circle is an 80-m tower and scanning lidar. Dashed blue lines indicate the angle of flow unobstructed by wind turbines for the prevailing wind direction (westerly).

AFFILIATIONS: Wilczak, Banta, Marquis, and White—National Oceanic and Atmospheric Administration/Earth System Research Laboratory, Boulder, Colorado; Stoelinga, McCaa, and Bickford—Vaisala, Inc., Seattle, Washington; Berg, Chand, and Shaw—Pacific Northwest National Laboratory, Richland, Washington; Sharp—Sharply Focused, LLC, Portland, Oregon; Bianco, Bonin, Choukulkar, Djalalova, Lantz, Long, McCaffrey, Olson, Pichugina, and Worsnop—Cooperative Institute for Research in Environmental Sciences, University of Colorado Boulder, and National Oceanic and Atmospheric Administration/Earth System Research Laboratory, Boulder, Colorado; Bodini and Friedrich—Department of Atmospheric and Oceanic Sciences, University of Colorado Boulder, Boulder, Colorado; Clifton—WindForS, Stuttgarter Lehrstuhl für Windenergie, Institut für Flugzeugbau, Universität Stuttgart, Stuttgart, Germany; Cline—National Oceanic and Atmospheric Administration/National Weather Service, Washington, D.C.; Cook and Muradyan—Argonne National Laboratory, Lemont, Illinois; Draxl and Scott—National Renewable Energy Laboratory, Golden, Colorado; Eckman—National Oceanic and Atmospheric Administration/Air Resources Laboratory, Idaho Falls, Idaho; Leo, Fernando, Otarola-Bustos, and Krishnamurthy—Civil and Environmental Engineering and Earth Sciences, University of Notre Dame, Notre Dame, Indiana; Lundquist—Department of Atmospheric and Oceanic Sciences, University of Colorado Boulder, Boulder, and National Renewable Energy Laboratory, Golden, Colorado; Wharton—Lawrence Livermore National Laboratory, Livermore, California
CORRESPONDING AUTHOR: James Wilczak, james.m.wilczak@noaa.gov

The abstract for this article can be found in this issue, following the table of contents.
DOI:10.1175/BAMS-D-18-0035.1

Supplements to this article are available online (10.1175/BAMS-D-18-0035.2 and 10.1175/BAMS-D-18-0035.3)

In final form 4 April 2019

Table 1. Main observing sites within the core WFIP2 domain (other than the physics site). Boldface site names indicate supersites (magenta sites in Fig. 1), where several different types of complementary instruments were deployed. Radiation measurements are coded as follows: shortwave down (1), longwave down (2), shortwave up (3), longwave up (4), and net radiation (measured by a net radiometer) (5).

Site name	Radar wind profiler	RASS	Scanning lidar	Profiling lidar	Profiling sodar	Microwave radiation	Ceilometer	Microbarograph	Radiation	Surface meteorology	Soil temp and moisture	Soil heat flux
Forks, WA	×	×							1	×		
Astoria, OR	×	×							1	×		
North Bend, OR	×	×							1	×		
Troutdale, OR	×	×		×		×		×	1, 5	×		
Prineville, OR	×	×			×				1, 2, 3, 4, 5	×	×	×
Yakima, WA	×	×			×					×		
Condon, OR	×	×			×	×		×	1, 2, 5	×		
Walla Walla, WA	×	×			×			×		×		
Goldendale, WA	×	×			×			×		×		
Goldon Ridge, OR			×	×	×							
Rufus, OR					×	×		×	1, 2	×		
Wasco, OR	×	×	×	×	×	×	×	×	1, 2, 3, 4, 5	×		
Boardman, OR	×	×	×		×			×	1,2, 3, 4	×	×	×
Bonneville, OR								×		×		
Hood River, OR								×		×		
Oreg Raceway Track, OR					×							
Decker Ranch, OR					×							
Arlington, OR			×	×								
Umatilla, Or								×	1	×		
Vansycle Ridge, Or				×								
Gilhouley Road, OR					×							
Shell Rock Road, OR					×							
15 Mile Road, OR					×							
Van Gilder Road, OR					×							
Old Tree Road, OR					×							
Sand Hollow Road, OR					×							
Plymouth, WA					×							

along the Columbia River at similar elevations, while Goldendale, Washington and Rufus, the physics site, Wasco, and Condon, Oregon, form a transect almost perpendicular to the river with elevations differing by almost a kilometer.

Table 1 summarizes the instruments deployed at each of the observing sites, with supersites highlighted in boldface. At these sites complementary instrument systems provided a comprehensive depiction of key meteorological phenomena and processes (Wasco, the main observing site, had nine systems), allowing for a thorough evaluation of model skill at simulating those processes.

The physics site (red star, Fig. 1c), as the finest-scale, innermost observational domain, was meant to approximate a single high-resolution model grid cell. The site, located just west of a wind farm (Fig. 2), included a network of 12 towers that measured surface flux and wind speed variability. The towers spanned an area approximately 2 km × 2 km, forming both east–west and several north–south transects. On the east side of the physics site, a scanning Doppler wind lidar complemented an 80-m tower that had two pairs of sonic anemometers (on north- and west-facing booms) at 50 and 80 m above ground level (AGL). A wind-profiling sodar and surface energy budget instruments anchored the

Table 2. Instrumentation within the physics site; *T* is temperature and RH is relative humidity.

Tower location	Anemometer heights (m AGL, sonic unless noted)	Other parameters (m AGL, high-frequency unless noted)
P01	3, 10	*T*, RH (3, 10); pressure, CO_2, H_2O (3)
P02	3, 10, 17	*T*, RH (3, 17); pressure, CO_2, H_2O (3)
P03	10	*T* (10)
P04	10	*T* (10)
P05	10	*T* (10)
P06	3, 10, 21	*T*, RH (3, 21); pressure, CO_2, H_2O (3)
P07	3 (prop and vane)	*T*, RH, pressure (2) (1-min frequency)
P08	3 (prop and vane)	*T*, RH, pressures (2) (1-min frequency)
P09	10	*T* (10)
P10	10	*T* (10)
P11	3, 10	*T*, RH (3, 10); pressure, CO_2, H_2O (3)
P12	40, 80 (two at each height)	*T* (40, 80; two at each height)
Other measurements		
P01	Sodar wind profiler (wind speed and direction up to 200 m) Moisture flux at 3 m Soil temperature and moisture profile Shortwave and longwave upward and downward radiation	
P03	Surface energy balance/Bowen ratio station	
P07	Shortwave downward radiation	
P12	Scanning lidar	

west side of the site. Table 2 describes the instruments at each physics site tower location. For prevailing westerly winds (between the two dashed blue lines of Fig. 2), the instruments were unwaked by turbines, while for less frequent easterly flow, the instruments provided measurements of potential turbine wake effects.

After completion of the field campaign, each group that deployed instrumentation created a quality-controlled (QC) version of their datasets. The QC procedure typically involved two steps: first, applying automated algorithms to identify and remove outliers and, second, a visual inspection of the data with hand editing of the data as necessary. The original raw data, QC data, derived data, and accompanying metadata including QC procedures, as well as model simulation output, are all available from the DOE Data Archive and Portal (DAP) described in detail in the companion WFIP2 paper in this issue (Shaw et al. 2019). Instrument metadata includes information such as location, dates of deployment, data-processing methods including time averaging, whether the data were transferred to the NOAA Meteorological Assimilation Data Ingest System (MADIS) (https://madis.noaa.gov/support_overview.shtml), and whether the data were assimilated in real time into developmental versions of the Rapid Refresh (RAP) and High-Resolution Rapid Refresh (HRRR) models run at NOAA/Earth System Research Laboratory (ESRL). A condensed list of instrument metadata appears in the online supplementary material (Table ES1; https://doi.org/10.1175/BAMS-D-18-0035.2).

In addition to standard measured meteorological parameters, derived data products were also available from several of the instrument systems. In particular, convective boundary layer depths were determined from the 915-MHz RWPs (Bianco et al. 2008), and day and nighttime boundary layer depths were derived from the lidars at Wasco and Arlington (Bonin et al. 2017) (see sidebar). Furthermore, the Wasco RWP operated in a special mode for 30 min each hour that was optimized for estimating the turbulent kinetic energy dissipation rate (McCaffrey et al. 2017).

Auxiliary datasets collected during the WFIP2 field campaign were tall-tower, turbine nacelle anemometer, and turbine power output data provided by industry partners. Also, the NOAA/National Weather Service launched supplemental radiosondes during special observing periods at five sites (Quillayute and Spokane, Washington; Salem and Medford, Oregon; and Boise, Idaho), also available through MADIS.

The WFIP2 campaign provided an opportunity to develop or improve several data products from routine measurements made during the study.

Detection of range-folded returns. Many lidar systems have high pulse repetition frequencies (10–20 kHz), which places a limit on the unambiguous range. Consequently, these systems are susceptible to range folding, which occurs when returns from a previous pulse contaminate returns from the current pulse. A new method that identifies and removes this range folding has been developed using WFIP2 observations (Bonin and Brewer 2017).

Extending vertical coverage of mean wind measurements. A method that significantly improves the vertical coverage of wind measurements from scanning Doppler lidars (Fig. SB1) by accumulating the spectra from all the beams of the scan (Smaliko 2003) has been adapted for ground-based lidars. This technique reduces the noise in the spectra, making the spectral peak stand out. This technique was especially useful during cold pool periods dominated by clean, low-aerosol air.

Two-dimensional wind transects. A novel technique using scanning-lidar data to retrieve two-dimensional wind transects has been developed that uses high-density, low-level measurements to retrieve the horizontal wind fields over a horizontal domain. This is done by binning the line-of-sight measurements in the horizontal and the vertical and performing a 2D retrieval within each bin. The retrieval results allow for visualization of the evolution of the flow over horizontal transects, which is useful to study the influence of complex terrain or wind plant wakes.

Calculation of TKE dissipation rate. The turbulence dissipation rate ε was measured using four methods on three remote sensing instruments at Wasco, and compared to a nearby sonic anemometer (5.8 km north and 40 m higher in elevation) from the 80-m tower at the physics site. The profiling-lidar estimated ε from the variance of the measured line-of-sight velocity (Bodini et al. 2018). For the 915-MHz RWP, ε was calculated using the width of the velocity spectra from the vertically pointing beam (McCaffrey et al. 2017). The scanning Doppler lidar estimated ε using (i) a structure function method on the planned position indicator scans (Frehlich et al. 2006; Krishnamurthy et al. 2011) and (ii) a spectral-slope method on the vertical stares.

Figure SB2 shows comparisons at 80 m AGL (top panel), of the sonic anemometer and the three methods available, and at 200 m AGL (bottom panel), where all three remote sensing instruments overlap and the four methods can be compared. Although the agreement between instruments and with respect to the reference estimate from the sonic anemometer varies throughout the day, changes in the dissipation rate over the course of a day are often captured well.

Determining mixing-layer height. Measurements from RWP and scanning Doppler lidars were used to measure the convective boundary layer depth during WFIP2. For the RWPs, automated estimates of mixing-layer height (MLH) were determined first using only the signal-to-noise ratio (SNR), and second by combining the SNR with hourly values of vertical velocity variance and spectral width (Bianco et al. 2008). For the scanning lidars, the MLH was calculated as the maximum height at which turbulent mixing occurs that is connected to the surface (Bonin et al. 2018), incorporating information on turbulent quantities and gradients of mean variables. Estimates of the uncertainty are also made, related to the spread in the turbulent and mean profiles input into the algorithm. An example of how these methods performed at Wasco (Fig. SB3) shows good agreement during daytime. Lidar estimates of boundary layer heights are also available at nighttime. An extensive intercomparison over the entire campaign is in progress, as is a comparison of the observed values with model-derived values.

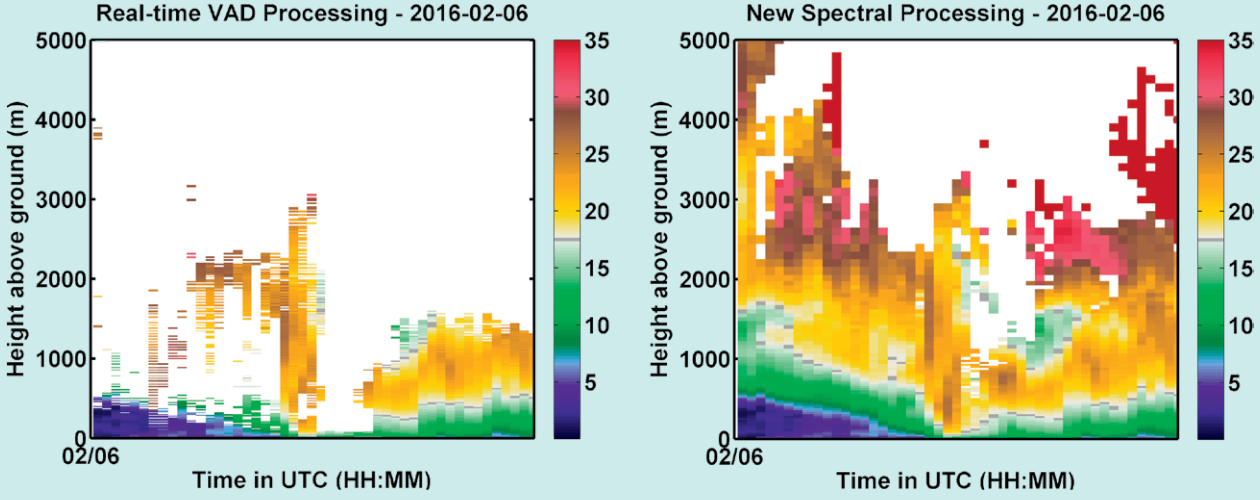

Fig. SB1. Example of a wind speed time–height cross section using (left) the standard VAD and (right) the spectral averaging technique for Doppler lidar winds from data collected at Arlington on 5–6 Feb 2016.

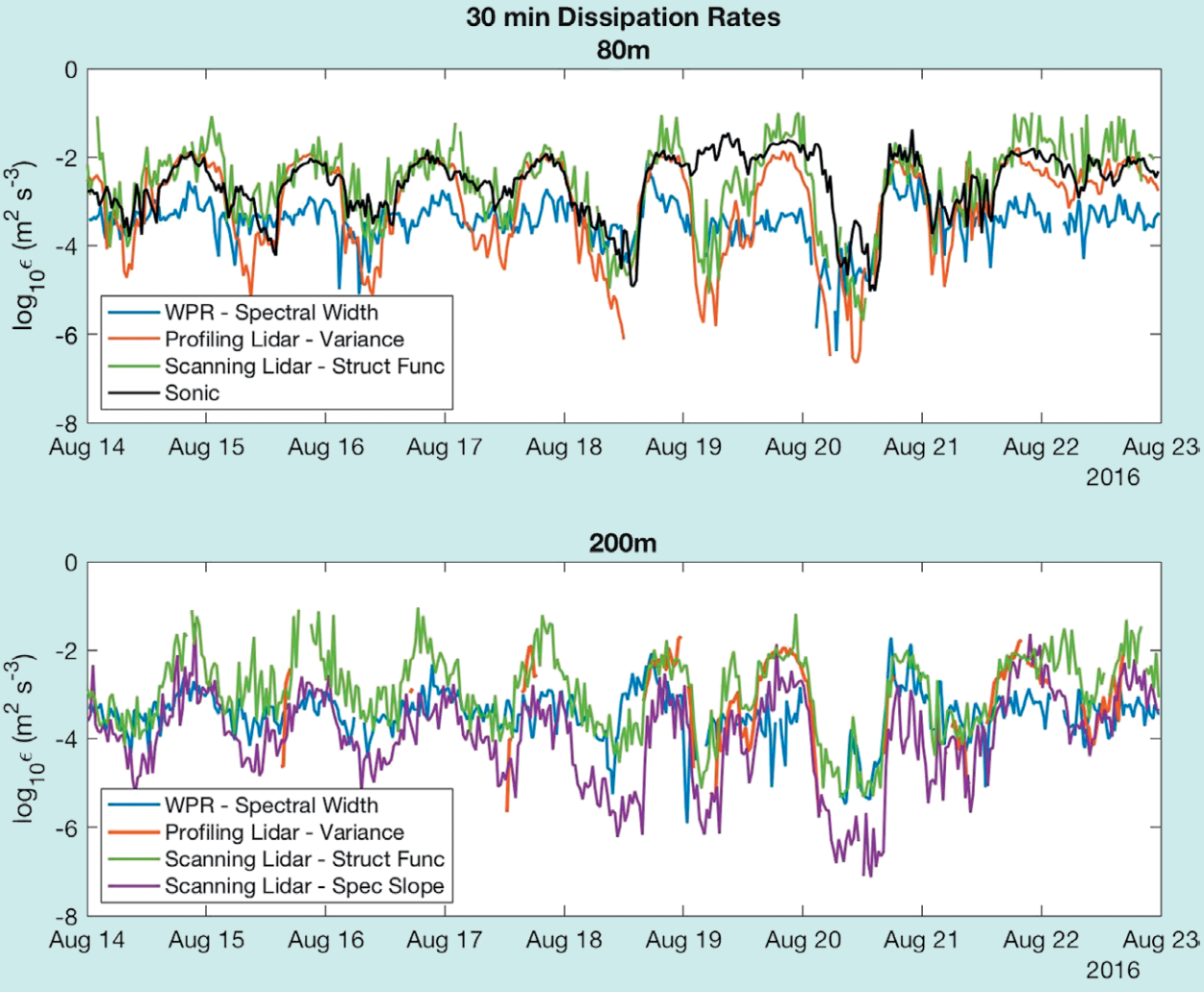

Fig. SB2. Turbulence dissipation rates at Wasco from the radar wind profiler (blue), profiling lidar (red), and scanning lidar using the structure function (green) and spectral slope (purple) methods at two heights: (top) 80 m AGL, compared to the sonic anemometer 5.8 km away at the physics site (black), and (bottom) 200 m AGL.

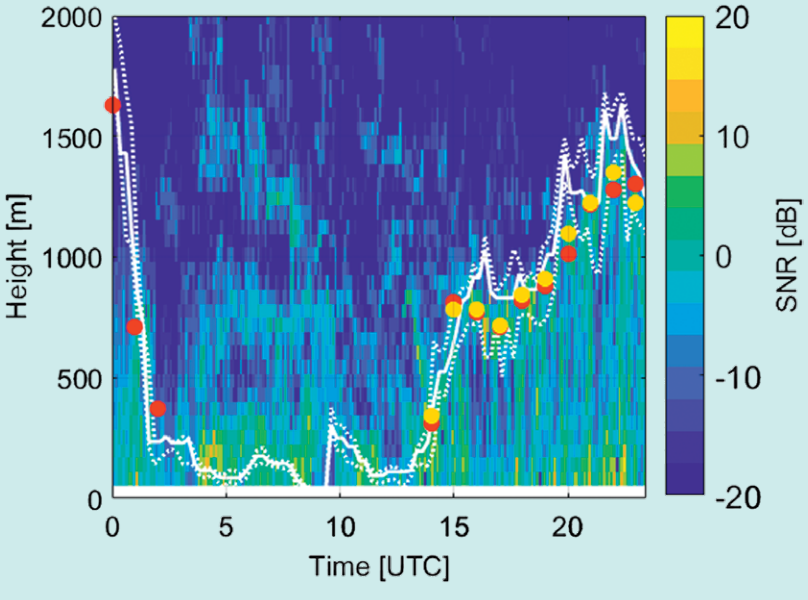

Fig. SB3. Doppler lidar MLHs (white solid line) with uncertainty (white dashed lines) along with RWP MLHs using the SNR method (red dots) and composite method (orange dots) overlaid on the RWP SNR on 21 Jun 2016.

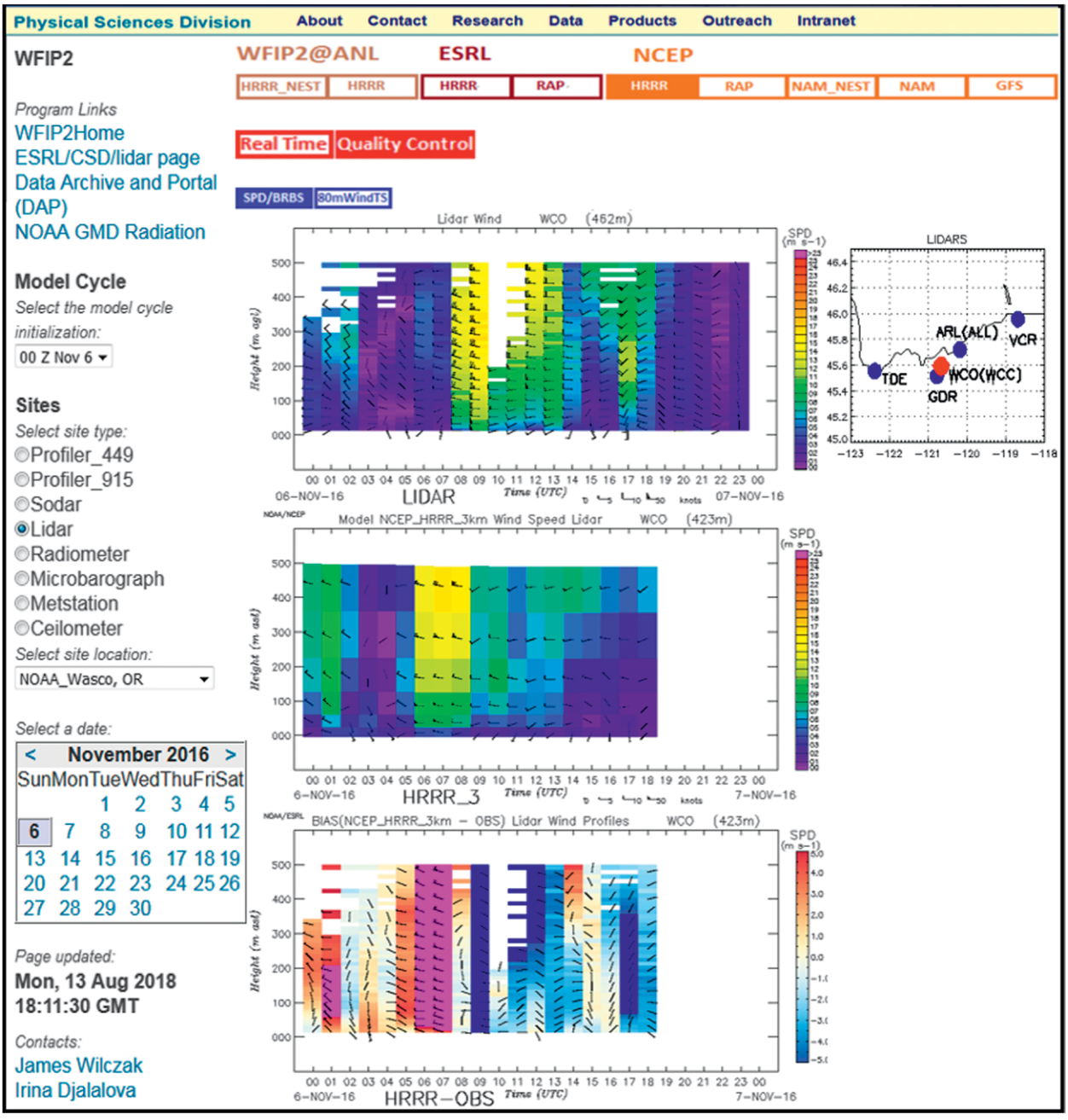

Fig. 3. Observation–model evaluation website allowing for comparisons between observations and forecasts in real time or using historical data. In this example the three panels show 24-h time–height cross sections of wind barbs and speed at Wasco, OR of (top) lidar, (middle) NCEP HRRR model, and (bottom) differences between the first two panels (model minus observations).

OBSERVATION–MODEL EVALUATION WEB TOOL. To facilitate rapid progress in improving the forecast models through use of the observations, a real-time model–observation evaluation web tool (http://wfip.esrl.noaa.gov/psd/programs/wfip2/) was developed. This tool (Fig. 3) was used on a daily basis by instrument owners to ensure their instruments were running correctly; by observationally oriented project scientists to understand the meteorological phenomena that had a large impact on wind energy; and by modelers to see, in real time, forecast busts together with detailed observations of the phenomena that contributed to those busts. For a complex field campaign such as WFIP2, the capability provided by this tool made an essential contribution to the program's success. This site also supported the construction of the event log (discussed below) and selection of case studies, and it continues to be used for data analysis.

On the web page, users can choose the instrument type; select different displays of data available for the particular instrument system, such as wind, temperature, relative humidity, and signal-to-noise ratio; view the original real-time observations or QC data; select the model initialization time (the start hour of the images); and choose the site and date of interest. The web tool also allows users to select from nine different NWP models to compare to the observations. For profiling instruments, the web page has three panels, as illustrated in Fig. 3, showing the observations, corresponding model data, and their difference. In situ instrument data are displayed as time series of the observations overlaid with the model forecasts (not shown). In addition, the website provides links to the DAP and to ancillary websites for the NOAA lidar and radiation observations.

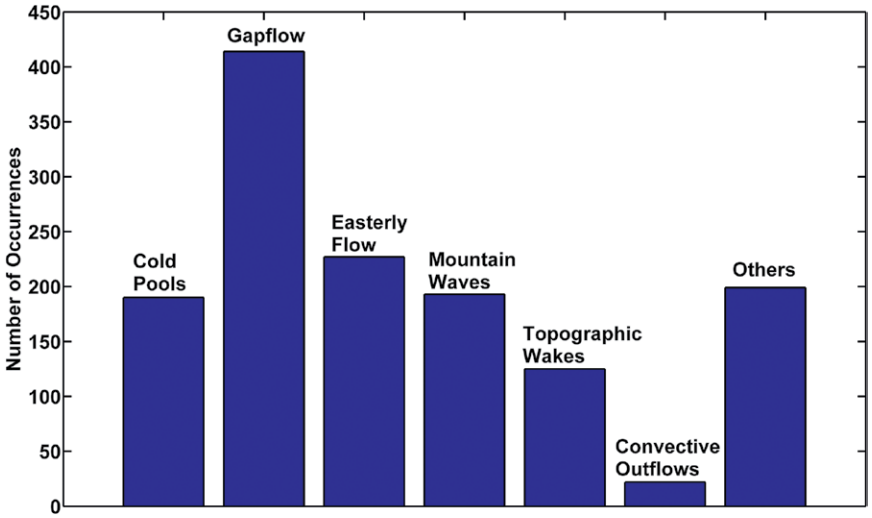

Fig. 4. Number of days that each type of event was observed during the WFIP2 measurement campaign. Multiple events can occur on the same day, for example, an easterly flow in the initiation phase of cold pools or a gap flow with mountain waves.

EVENT LOG. Each week throughout the field program, an online virtual meeting was held in which program scientists would review the previous seven days of weather in the region. In addition to the field campaign observations, simulations from the real-time 13-km RAP, 3-km HRRR, and 750-m HRRR nest models (see Olson et al. 2019) were discussed. Additional data products utilized were global model forecasts, satellite imagery, local National Weather Service (NWS) soundings and surface observations, and time series of aggregate wind power generation within the regional grid operator's [Bonneville Power Administration (BPA)] balancing area (https://transmission.bpa.gov/Business/Operations/Wind/twndbspt.aspx). The BPA area spans all of Washington, Oregon, and Idaho plus portions of five other states, covering more than 750,000 km^2. Although the total capacity within the entire BPA geographic boundary is over 6 GW, at the time of WFIP2, the BPA controlled approximately 4.6 GW of that capacity on their system. For each day, a brief synopsis of the weather was written, assessing the significance of the key phenomena and their impact on wind power generation, including cross-barrier westerly flow, cold pools and the mechanisms leading to their growth or decay, mountain waves and wakes, convective outflows, and easterly flow. In addition, the log included an indication of the performance of model forecasts. All of this information was recorded in the event log, available on the DAP.

METEOROLOGICAL PHENOMENA. The following three primary weather phenomena were identified as the focus for WFIP2 observational and model improvement efforts:

- Cold pools—These routinely develop within the Columbia basin east of the Cascades in the cold season as dense air settles into the lower elevations accompanied by stagnant or weak to moderate easterly flow. The mix out of these cold pools under transition to stronger westerly flow and the resulting upramp in wind power generation is one of the greatest challenges of wind energy forecasting in this region.
- Gap flows—These intense flows can occur any time of the year and can be either westerly or easterly. WFIP2 focused on warm-season, westerly gap flows primarily forced by inland daytime heating, but that can also be influenced by synoptic-scale transient weather patterns. These strong gap flows drive reliably large amounts of wind power production, but their onset and especially decay are not well predicted.
- Mountain waves and wakes—Under conditions of strong, deep westerly flow, primarily in the cold and transition seasons, flow over the Cascade crest

and its volcanic peaks produce mountain waves and topographic wakes that can extend hundreds of kilometers downwind. Shifts in the position and amplitude of these features can strongly affect production at individual wind farms.

Using the daily event log generated by the WFIP2 team during the study, we compiled statistics on the number of days each of these three types of events occurred during the 18-month field study (Fig. 4). We also show a count of days with atypical easterly flow, and with convective outflows. Convective outflows were anticipated to be an important phenomenon affecting wind energy, but they occurred infrequently. The final category, "other," refers to days in which additional phenomena outside these categories had an impact on wind energy. Figure 4 underscores the pervasiveness of gap flow events, which occurred on the majority of days during the field campaign, more than twice as often as cold pool and mountain wave/wake events.

The importance of local meteorology to wind energy generation in the Pacific Northwest, and the particular importance of gap flows and cold pools, is illustrated in Fig. 5. Here the normalized aggregate wind power production produced on the entire BPA system for 6-week summer (top panel) and winter (bottom panel) time periods are compared to the equivalent power calculated using remotely sensed 80-m winds observed at 22 independent WFIP2 sites (19 with sodars and 3 with lidars). The equivalent power is calculated by passing those winds through an IEC class 2 standard power curve (similar to most of the turbines in the area) to convert to wind power [see Wilczak et al. (2018) for details on the conversion]. The summer episode shows a pronounced diurnal variation of wind power through most of July, because of the daily formation of thermally driven gap flows through the Columbia River Gorge. Sharp up- and downramps of power occur on each day, with the total aggregate normalized power varying from near zero to near unity (100% of possible generation). In contrast, in winter (bottom panel), there are long episodes associated with cold pools where the aggregate power remains near zero continuously for up to a week. Clearly, the meteorological phenomena studied during WFIP2 have a profound impact on the aggregate wind power generation over the entire BPA system area, and this motivates our desire to understand their dynamics and to forecast them accurately. In addition, we note that the high correlation between the BPA aggregate power and that derived from the 22 WFIP2 remote sensing 80-m sites indicates that the WFIP2 sites are representative of the meteorology affecting the regional wind energy

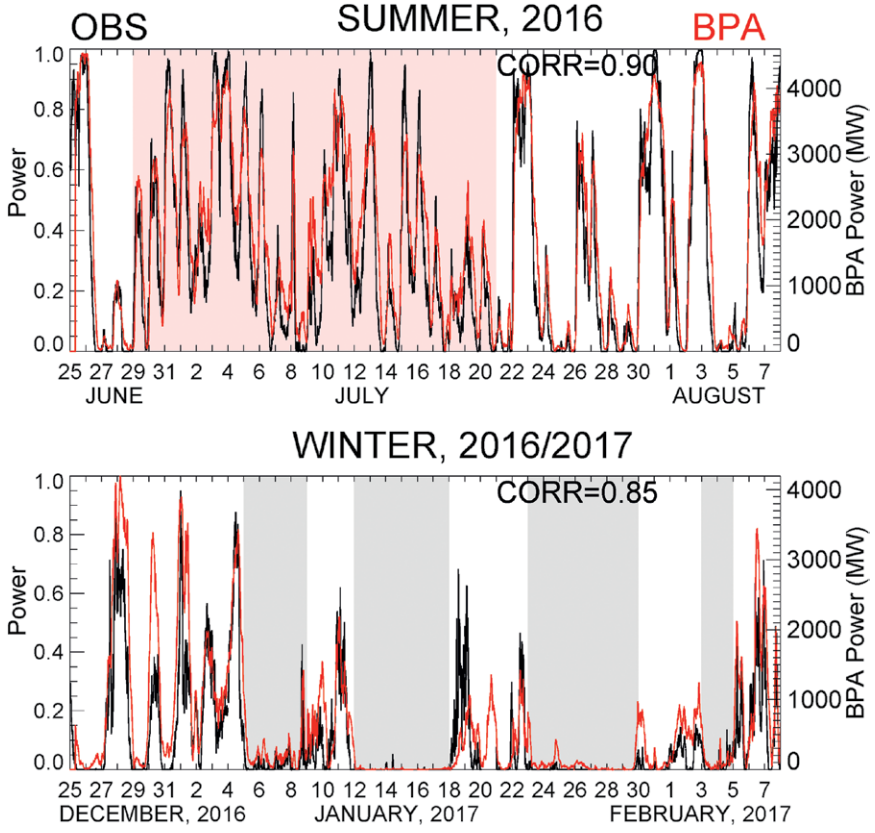

Fig. 5. Time series during (top) summer and (bottom) winter of normalized aggregate wind power generation on the Bonneville Power Administration system (red curves) and the aggregate equivalent power derived from a network of 22 WFIP2 remote sensing sites that measured 80-m winds (black curves). Red-shaded area shows times in summer with strong diurnal gap flows, and gray-shaded area shows times in winter with stagnant winds during cold pools. The high correlation coefficients (R = 0.90, 0.85) indicate the WFIP2 observations sites are a good surrogate for all of the wind farms present on the BPA grid.

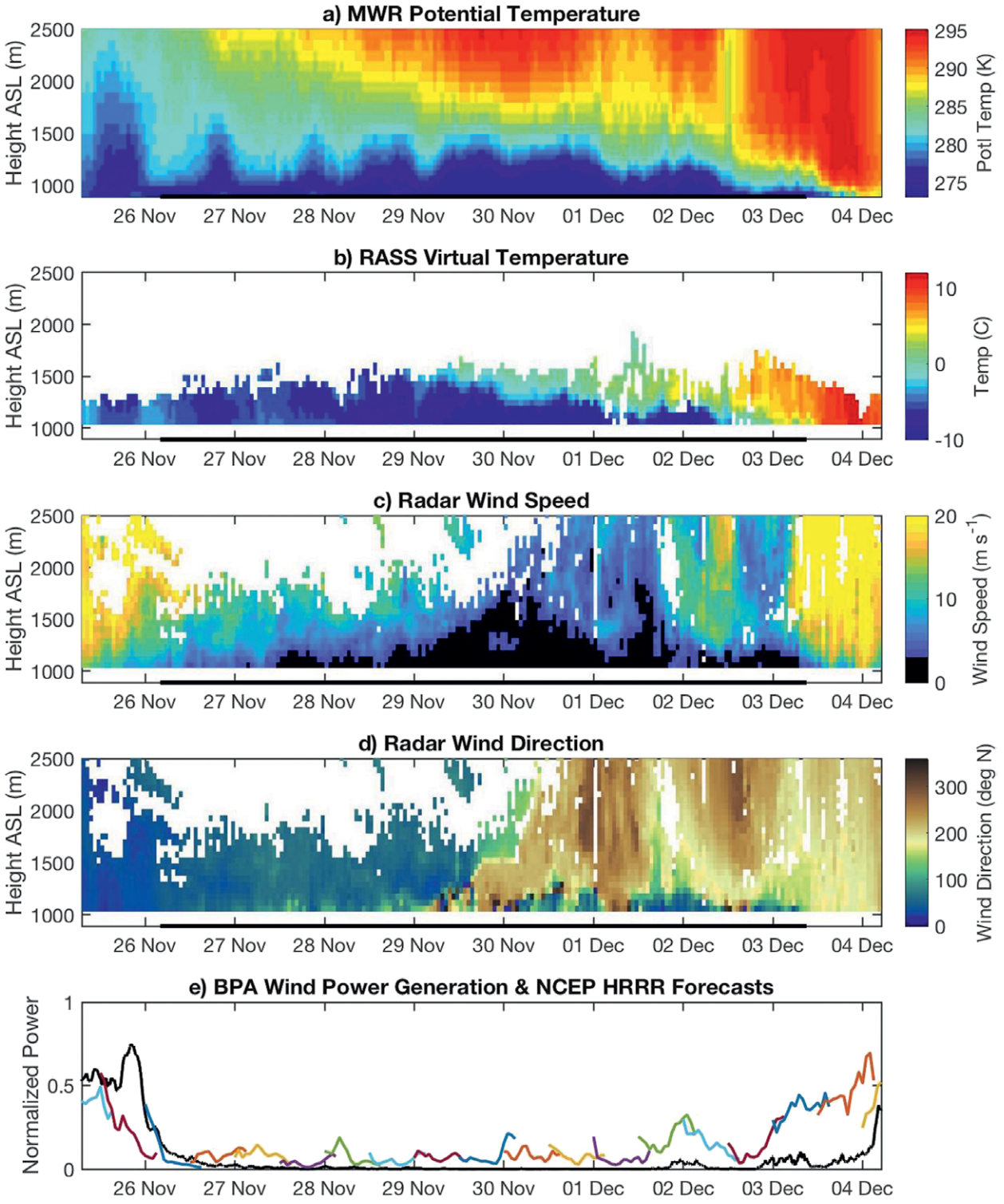

Fig. 6. Time–height cross sections at Condon, OR, between 25 Nov and 4 Dec 2015, spanning the life cycle of a cold pool event: (a) microwave radiometer potential temperature, (b) RASS temperature, (c),(d) radar wind profiler horizontal wind speed and direction from its high-resolution mode with speeds less than the 3 m s^{-1} turbine cut-in speed shaded black, and (e) wind power generation in the Bonneville Power Administration region (black line) and equivalent wind power aggregated at 22 remote sensing WFIP2 sites from 0000 and 1200 UTC NCEP HRRR model forecasts (colored lines). White areas in the profiling measurements indicate no data due to lack of signal strength.

generation. As a result, improvements to model forecasts evaluated at these 22 sites, as discussed in Olson et al. (2019), will be indicative of the wind power forecast improvements that the local grid balancing authority (BPA) would experience if they were to use these improved forecasts. Next we discuss in more detail the physical processes and model skill associated with the three meteorological phenomena that were the main focus of WFIP2: cold pools, gap flows, and mountain waves/wakes.

Cold pools. The Columbia River basin is surrounded by higher terrain on all sides. Because of this, cold pools with weak winds frequently settle into the basin during the winter months (Whiteman et al. 2001, Zhong et al. 2001), resulting in periods with little to no wind energy production. Under weak pressure gradient conditions, cold pools can form as a result of radiatively driven cold air drainage. Cold pools can also be initiated by northerly/easterly cold-air advection (Sharp and Mass 2002, 2004), which can then be blocked by the Cascades. In this case, the cold pool typically deepens as the easterly inflow exceeds the outflow of cold air exiting through the Columbia River Gorge to the west. Eventually the surface pressure gradient comes into equilibrium, producing stagnant winds. In the later stages of a cold pool's life cycle, strong southerly to southwesterly flow is typically present aloft prior to the approach of a cold front, with strong wind shear at the top of the cold pool. The cold pool remains intact until either turbulence in the shear layer erodes the pool away from the top, or daytime radiative-forced mixing undermines the cold pool from below. When high momentum air finally mixes to the surface, a rapid ramp in wind energy production occurs. The timing of this erosion is therefore crucial for wind energy production but is difficult to forecast.

A typical example depicting the evolution of such a cold pool occurred between 25 November and 4 December 2015 (Fig. 6). At the beginning of the event, 500-hPa flow over the region exhibited strong ridging into the Gulf of Alaska, while at the surface, high pressure over British Columbia migrated south into the Columbia basin, resulting in robust easterlies and rapid deepening of cold air. The brisk easterly flow weakened from the surface upward between 26 and 29 November (Figs. 6c,d), as the region east of the Cascade Crest filled with cold stable air and windward ridging neutralized the surface pressure gradient. By 0000 UTC 26 November, the wind below 200 m dropped to levels barely sufficient to generate wind power (Fig. 6e), and this low level of power generation continued for the next seven days. During this time period, a distinct diurnal signal (Fig. 6a) from surface mixing during short but sunny days failed to mix out the cold pool.

The upper ridge slowly migrated inland, and, by 30 November, yielded a deep layer of cold, stagnant air over the study region (Figs. 6a–d). At the same time, warmer air arrived above the cold pool because of both subsidence and advection, thus strengthening the atmospheric static stability at the inversion (Figs. 6a,b) and reducing the depth of the cold pool between 30 November and 2 December. Meanwhile, an upstream trough undercut the ridge from the west, bringing increasingly strong and warm southerly winds above the inversion on 2–3 December. Finally, a cold front aloft crossed the Cascades early on 4 December, reducing the static stability and allowing increased mixing within the lower layer, resulting in strong warming at the surface and a rapid increase of wind speed (Figs. 6a–c).

A significant challenge for wind energy facilities in the Columbia River basin is forecasting the ramp up of wind energy as the approaching synoptic-scale system overruns the stable cold air pool, gradually eroding the cold pool and mixing momentum downward from aloft. NWP models typically overmix the boundary layer (Smith et al. 1997a; Reeves and Stensrud 2009), resulting in too rapid a descent of high-momentum air down into the turbine rotor layer. This can be seen in Fig. 6e, where the 0000 and 1200 UTC forecasts of equivalent power (derived at the 22 WFIP2 remote sensing sites with 80-m winds) from the from the NOAA/NWS/National Centers for Environmental Prediction (NCEP) operational HRRR (version 2) are plotted in color, along with the actual amount of wind power on the BPA grid in black. The model runs continuously predicted slightly too much power until near the end of the event, when the last several model forecast cycles prematurely mixed out the cold pool completely and large forecast busts occurred.

Details of the overmixing process for a different cold pool event that occurred in February 2017 are shown through wind and temperature time–height cross sections in Fig. 7. Observations at Wasco (Fig. 7, top row) show a sharp vertical gradient of wind speed, wind direction, and temperature, gradually descending with time. The operational HRRR model behavior (Fig. 7, middle row), over two model cycles, shows a more diffuse upper boundary to the cold pool, and excessive downward mixing of southwesterly wind and warm air. The differences (model minus observations; Fig. 7, bottom row) show a clear high bias in wind speed within and at the top of the cold

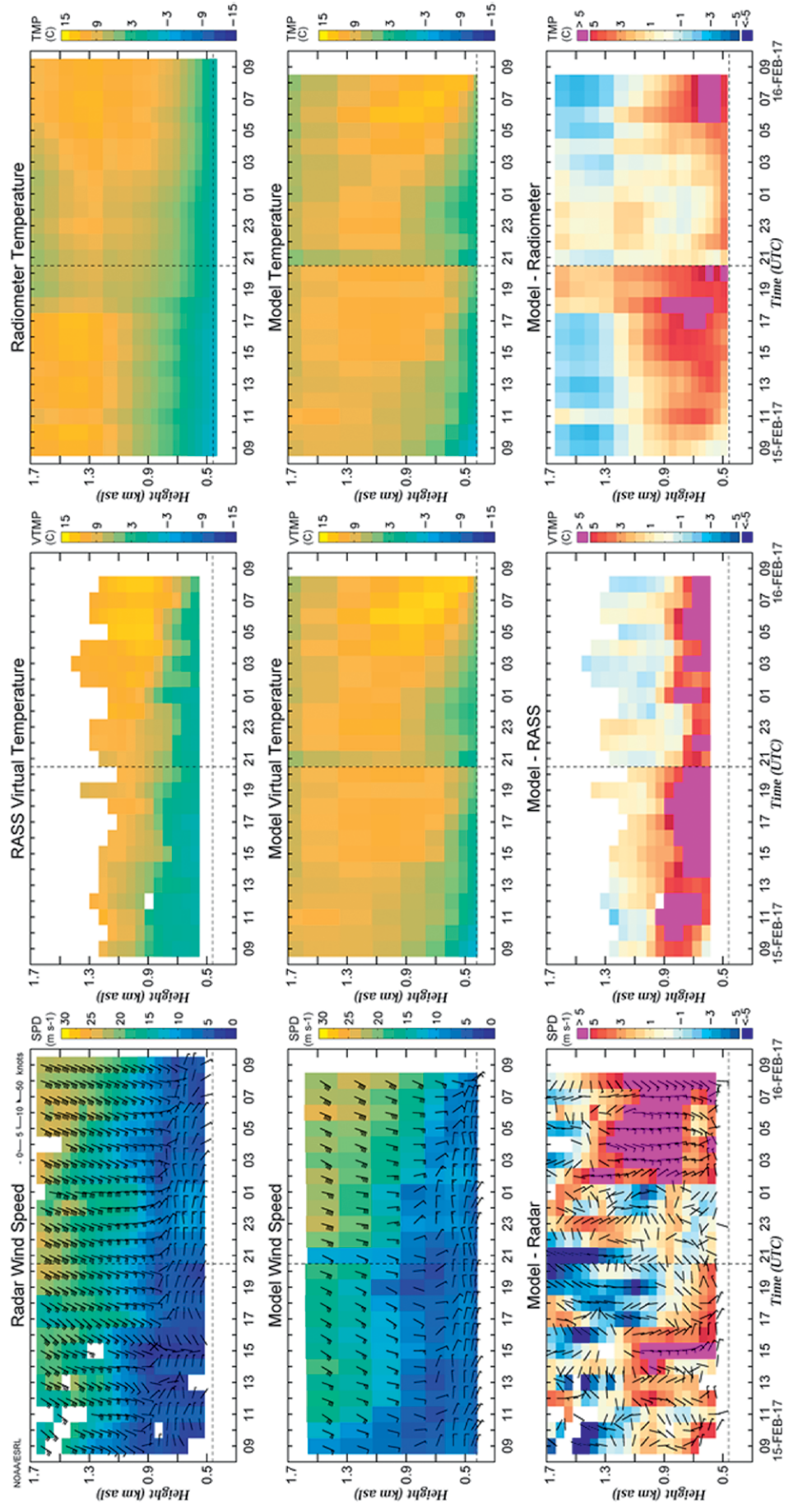

Fig. 7. Time–height cross sections of (left) horizontal winds, (center) RASS virtual temperature, and (right) microwave radiometer temperature [(top) observed, (middle) predicted, and (bottom) predicted minus observed] at Wasco for two NCEP HRRR forecast cycles initialized at 0900 and 2100 UTC 15 Feb 2017 (indicated by the vertical dashed line). Horizontal dashed line indicates ground level. Local standard time (LST) = UTC – 0800.

pool, and a much-too-warm temperature bias. The model's struggle to capture the mixing process is highlighted by a discontinuity in the temperature structure from 2000 to 2100 UTC 15 February, when the new forecast is initialized. The previous model run had nearly completely eroded the cold pool, which is still prominent in the observations. The new model run is provided a "fresh start" with an updated cold pool, and then the model immediately proceeds to overmix again, and incorrectly dissipates the cold pool by around 0800 UTC 16 February. This behavior illustrates a common failure mode of NWP models.

Gap flows. The Columbia River Gorge has a major controlling impact on wind flow in the WFIP2 study region. As the only sea level gap through the Cascade Range, the pressure gradient across the mountain barrier determines the direction and strength of the flow through the gap (Sharp and Mass 2002, 2004 Mass et al. 1986). High pressure offshore to the west, frequently occurring during summer, forces westerly flow through the gorge and into and across the basin. Conversely, high pressure east of the Cascades and low pressure offshore produces an easterly flow through the gorge. In winter, these conditions often generate a cold pool that drains through the gorge, causing an easterly gap flow, which can lead to dangerous freezing rain and other inclement weather in the Portland, Oregon, area (Sharp and Mass 2002, 2004).

During the cold season, synoptic pressure systems, including traveling shortwave ridges and troughs, dominate the pressure-driven winds in the study area, creating both easterly and westerly gap flows. Doppler lidar time–height cross sections at Wasco, Arlington, and Boardman for a 2-day period (Fig. 8) illustrate both directions of gap flows. A trough axis passed through the study area, reversing the pressure gradient from higher pressure inland to the east to higher pressure offshore to the west around 2300 UTC 8 April. The resulting winds below 500 m

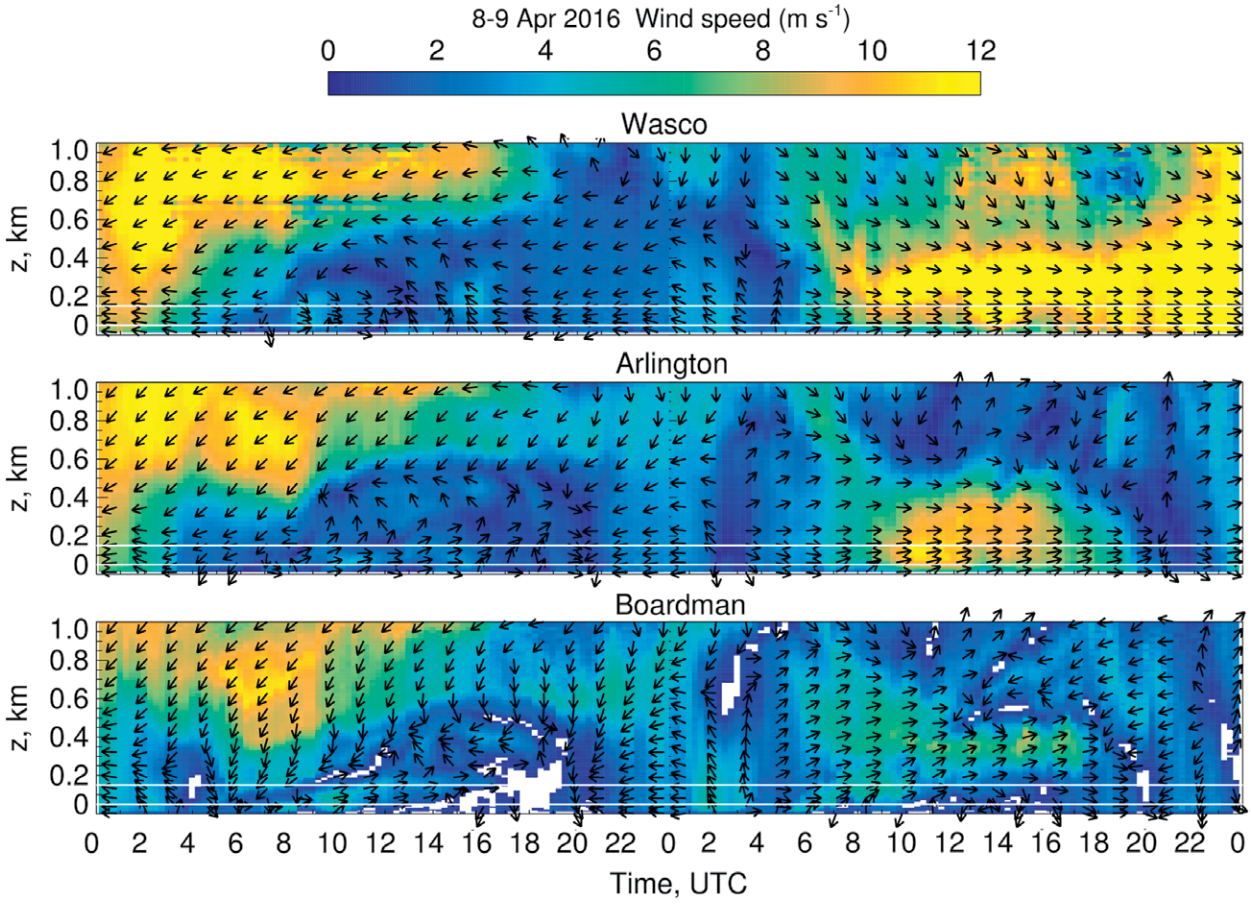

Fig. 8. Time–height cross sections (km AGL) of horizontal wind speed (colors) and wind direction (black arrows) at the (top) Wasco, (middle) Arlington, and (bottom) Boardman sites during easterly gap flow on 8 Apr and westerly gap flow the following day, 9 Apr 2016, illustrating vertical, temporal, and spatial (between sites) wind flow variability. Two white horizontal lines in each panel indicate heights of 50–150 m AGL, approximating a wind-turbine rotor layer. White areas indicate no data because of lack of signal strength.

shifted from a weak easterly gap flow prior to 0400 UTC 8 April to a stronger westerly gap flow after 0600 UTC 9 April. During the period of easterly flow, a RWP at Troutdale (west of the Cascades) observed a strong easterly gap outflow reaching 15 m s^{-1} at 500 m AGL in the exit region of the Columbia River Gorge (not shown). To better predict these easterly gap flow winds in the Portland area, especially during winter freezing rain events, Neiman et al. (2018) developed a gap flow tool combining observations from the Troutdale instruments.

In summer, the typical pressure pattern consists of a northward extension of the subtropical ridge offshore with lower pressure inland. In addition, hot daytime temperatures inland, often exceeding 30°C, can generate a diurnally varying pressure gradient via the sea-breeze mechanism. In the absence of transient synoptic forcing, the superposition of the diurnally varying pressure gradient with the mean onshore pressure gradient will produce a diurnally varying westerly gap flow through the gorge, as shown previously in Fig. 5. Lidar winds from three consecutive days at Wasco and Boardman (28–30 June, Fig. 9), indicate that typically the winds reach peak speeds near local midnight (0800 UTC), weakening the following morning. These gap flow winds cover a large area and can extend far downwind from the mouth of the Columbia River Gorge (Wasco and Boardman are approximately 50 and 120 km east of the mouth of the gorge, respectively). Differences in the depth, duration, and intensity of the gap flows at the two sites are likely due to their relative distance from the Columbia Gorge and to the elevation difference between the sites (Wasco being 350 m higher). Because of the broad area that the gap flows span, large diurnal variations in wind power generation occur on the BPA grid (Fig. 9c), with peak wind speeds strong enough that aggregate wind power generation can reach close to 100% of capacity

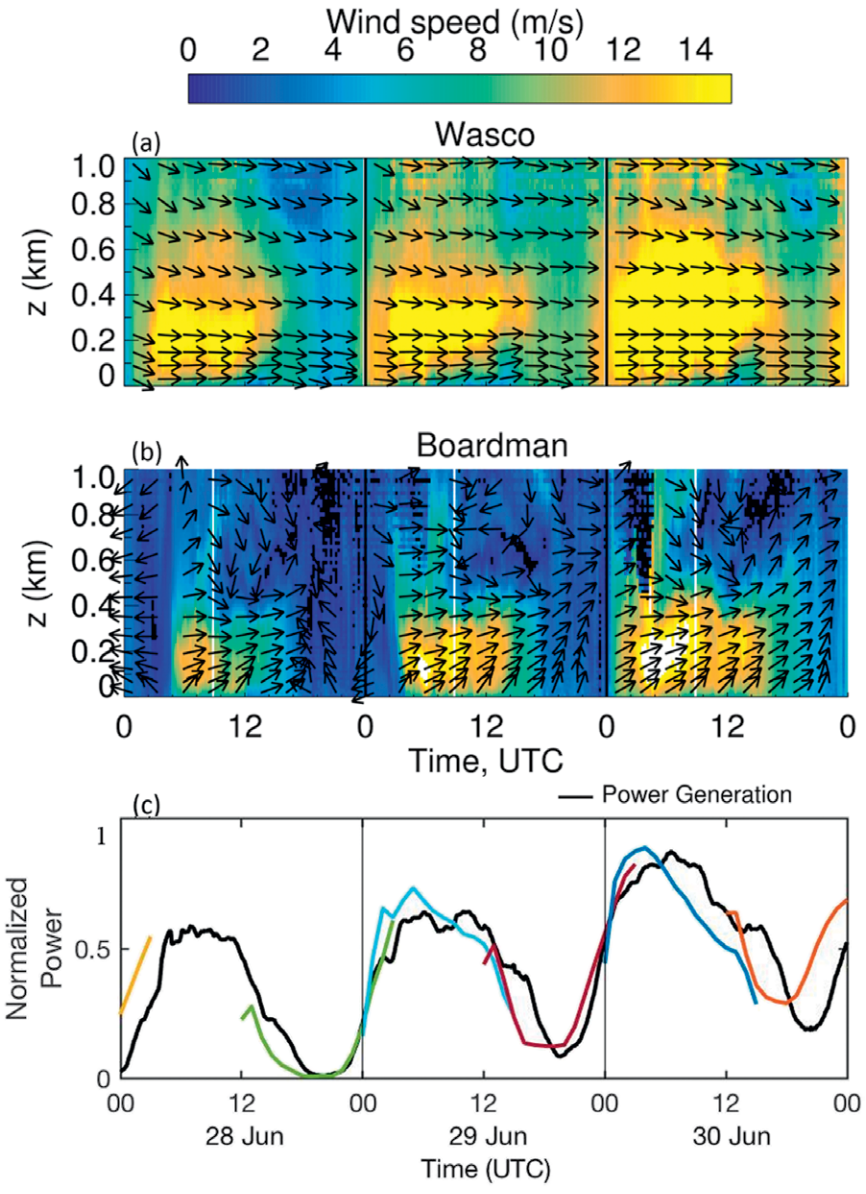

Fig. 9. Time–height cross sections (km AGL) of horizontal wind speed (colors) and wind direction (black arrows) at the (a) Wasco and (b) Boardman sites for 28–30 Jun 2016, showing the recurrent diurnal gap flow patterns due to sea-breeze forcing. (c) Total power generated over the BPA grid balancing area for this period (black line) and equivalent wind power aggregated at 22 remote sensing WFIP2 sites from 0000 and 1200 UTC operational HRRR model forecasts (colored lines). The elevation of Wasco is 462 m MSL, while Boardman is 112 m MSL. Local midnight (Pacific standard time) = 0800 UTC and local noon = 2000 UTC.

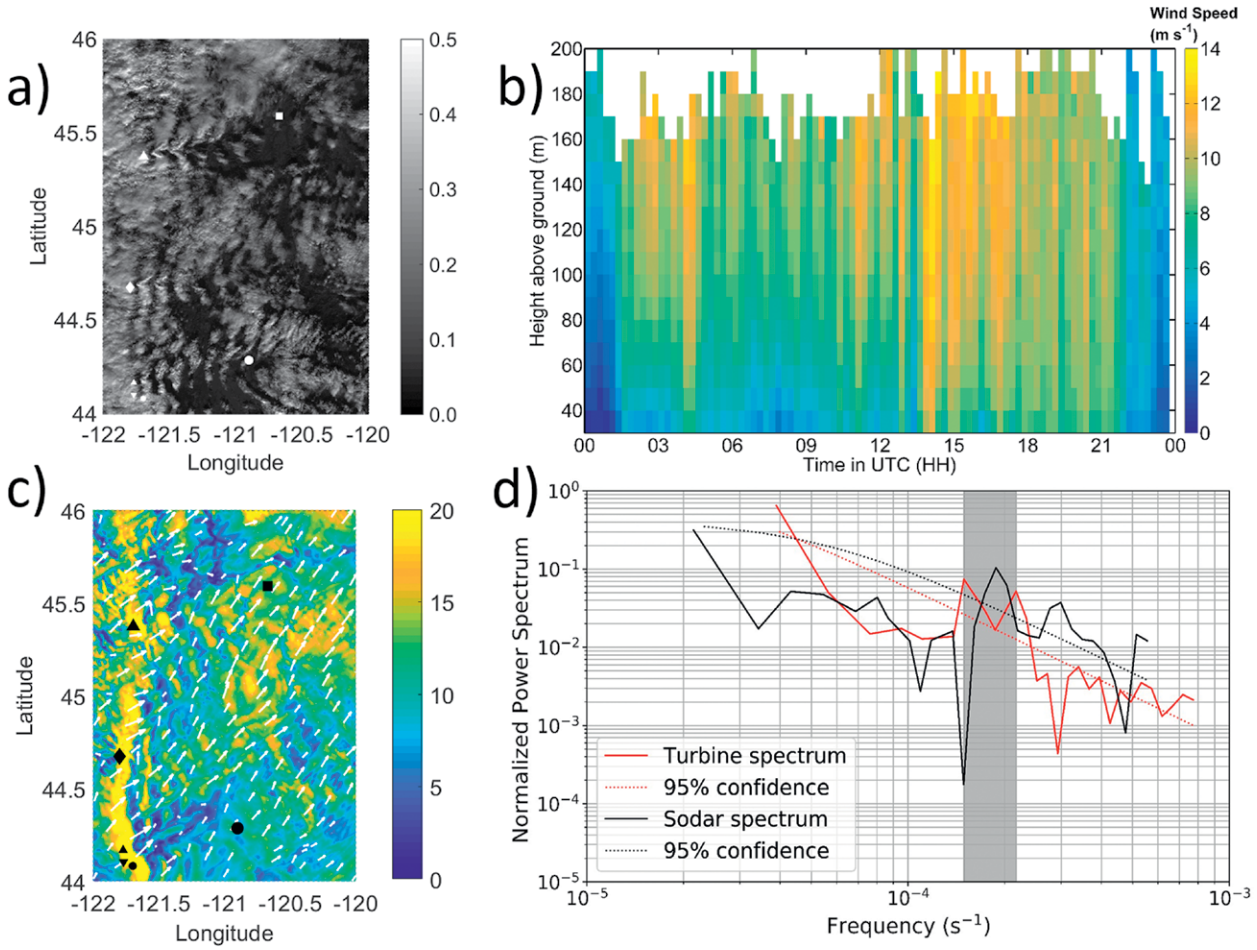

Fig. 10. Mountain-wave signatures observed on 12 Nov 2016. (a) MODIS *Terra* satellite reflectance (W m^{-2} μm^{-1} sr^{-1}) at 620–670 nm (250-m resolution) (b) The 15-min-averaged wind speeds from the Prineville sodar from 0000 UTC 12 Nov to 0000 UTC 13 Nov 2016. (c) Simulated 80-m wind speed from the control version of the HRRR nest (750-m grid spacing), all at 1845 UTC 12 Nov 2016. (a) and (c) are at 1845 UTC 12 Nov 2016. The bigger triangle pointing upward, square, diamond, and circle denote locations of Mount Hood, Wasco, Mount Jefferson, and Prineville, respectively. Sisters and Broken Top Mountains, located in the lower-left corner, are shown by smaller triangles and a circle. (d) Normalized power spectra of wind power generated from a front-row turbine south-southeast of Wasco (solid red) and from power estimates from the 80-m wind speeds observed by the Prineville sodar (solid black). The sodar spectrum is calculated during 0000–2400 UTC 12 Nov 2016 and the turbine spectrum is calculated for the period during which power is produced by the turbine (1000–2400 UTC). Overlaid (dotted) are the 95% confidence levels relative to red noise spectra (not shown) fit to the turbine and sodar spectra. The color of the red noise confidence levels matches their corresponding power spectrum. Peak power associated with the mountain waves occurs between 1.49 and 2.17 × 10^{-4} Hz (1.3–1.9-h period, gray-shaded rectangle).

(equivalent to 4.6 GW). Also shown in Fig. 9c are the 0000 and 1200 UTC operational HRRR forecasts of equivalent power from the 22 remote sensing sites. The timing of the model gap flow upramps is too early on 28 June and at the end of 30 June, while the model downramps occur too early on all three days. The gap flow downramp timing error is a common deficiency seen in the model on most days during the summer.

Mountain waves and wakes. Over the past decade, the impact of mountain waves and wakes on wind power plant output in the Pacific Northwest has been anecdotally recognized by wind energy meteorologists, who expect additional power generation volatility when they are present. However, to our knowledge, there has been no observational proof that these events do in fact impact wind energy production in the Columbia River basin or anywhere else, either at point locations or in a spatially aggregated sense. The WFIP2 dataset is well suited for investigating these potential impacts.

When stably stratified air ascends a mountain barrier, such as the Cascade Mountains, it can trigger the generation of gravity waves, also called

mountain waves or trapped lee waves (Durran 1990, 2003). Mountain waves can manifest themselves as transverse bands of clouds that form on the crests of the waves, seen in satellite images as cloud bands downstream of the terrain. Moderate Resolution Imaging Spectroradiometer (MODIS) satellite images on 12 November 2016 (Fig. 10a) show the presence of mountain waves with wavelengths of ~10 km.

Most often, mountain waves are slowly evolving phenomena, so that the properties of the waves, such as the positions of the wave crests relative to the topography, vary only gradually over time. If mountain waves were strictly stationary, a wind speed time series from a single location would give no evidence of their presence. However, observations at fixed locations have been able to reveal the existence of trapped lee waves because of temporal variations in the lee wave pattern (Ralph et al. 1992; Bougeault et al. 1993). Indeed, a time–height cross section of wind speed from the Prineville, Oregon, sodar on 12 November 2016 (Fig. 10b) indicates a strong periodicity of ~1.5–2 h. The relationship between the Prineville sodar periodicity and mountain waves was examined by analyzing 15-min instantaneous Geostationary Operational Environmental Satellite (GOES) images and tracking the propagation of wave crests at the Prineville location. This analysis indicated the wave crests were propagating westward (upstream), also with a period of approximately 1.5 h. Nance and Durran (1997, 1998) investigated the impacts of changes in upstream mean-flow conditions and wave nonlinearities on temporal variations of the trapped wave field. Although both can generate temporally varying trapped waves, they suggest that the type of variability evident in the sodar and satellite images of Fig. 10, and also that in Fig. 13 of Bougeault et al. (1993), is likely generated by nonlinear wave interactions.

Mountain waves, their wavelengths, and approximate locations were successfully simulated with the 750-m HRRR nest on 12 November 2016 (Fig. 10c). Animations of model vertical velocities at 80 m AGL (Fig. ES1 in the supplemental material) also replicate a westward propagation of the wave crests in the vicinity of Prineville and Wasco, consistent with the Prineville sodar and satellite analyses.

An analysis of normalized power spectra from wind turbine power and sodar wind speed measurements (Fig. 10d) confirms that the mountain waves seen in the satellite imagery and the Prineville sodar time–height cross section coincide with wind turbine output variability. The power spectrum from wind power generated by a front-row turbine (i.e., not impacted by turbine wakes) located south-southeast of Wasco shows peaks in the spectrum between 1.49 and 2.17×10^{-4} Hz (1.3–1.9-h period). These peaks exceed the 95% confidence level of a red noise spectrum fit to the turbine power spectrum. The power spectrum calculated from sodar observations at Prineville[1] also shows significant spectral peaks within this frequency range with a maximum occurring at 1.87×10^{-4} Hz (1.5-h period). Thus, the frequency range of dominant energy is consistent with the period of mountain waves identified via satellite, establishing a direct connection between turbine power, sodar wind speed, and the wavelength of the mountain waves observed by satellite. To our knowledge, this is the first time the impact of mountain waves on wind energy production has been documented in the academic literature. This suggests that the presence of mountain waves should be considered when building wind farms in complex terrain: mountain waves impact not only the amount and location of the best wind resource, they directly impact wind resource quality by increasing temporal variability and reducing forecast skill.

While predicting the exact details of mountain waves may be difficult, the effects tend to cancel out across a large area, so that aggregation of wind power from a broad geographic area can greatly reduce the overall impact of the phenomenon. However, knowledge of the dominant wavelength and orientation of the wave field could help inform the design and layout of large wind farms in terrain prone to mountain waves such that the windward and leeward portions are equally exposed to the expected peaks and troughs of the mountain wave pattern. Finally, because mountain waves are more prevalent at certain times of year, they should be considered in energy system reserve planning.

In addition to mountain waves, large isolated mountains or islands can create wakes behind them

[1] Before calculating the sodar power spectrum, we first calculated wind power from the 80-m sodar wind speeds via a power curve defined for a turbine similar to the turbine near Wasco (i.e., similar hub height, rotor diameter, and rated power). All power spectra herein are calculated using Welch's method (Welch 1967), which estimates the power spectrum by dividing the detrended wind power time series into 50% overlapping segments with a Hanning window, computing a periodogram for each segment, and then averaging the periodograms. The spectra are then normalized by the sum of the power spectrum and smoothed by block averaging the spectra using 50 equally spaced, nonoverlapping bins of the logarithm of the frequency (Blackman and Tukey 1959; Piper and Lundquist 2004).

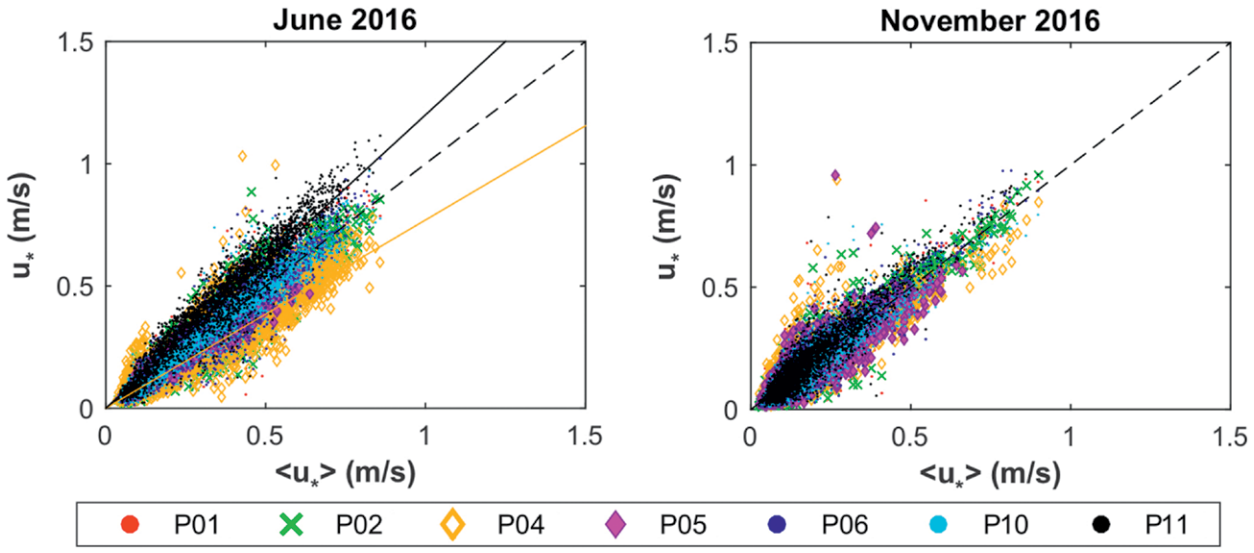

Fig. 11. Spatially averaged values of friction velocity $\langle u_* \rangle$ at 10-m height at the physics site vs local estimates of u_* at various physics-site tower locations (see legend) for the months of (left) June and (right) November 2016. The dashed black line represents a line with unitary slope and null y intercept, while the two solid lines represent slopes of 0.77 (yellow) and 1.2 (black), respectively.

with large areas of decelerated low-level flow (e.g., Smolarkiewicz and Rotunno 1989; Smith et al. 1997b; Wells et al. 2008). During WFIP2, mountain wakes often occurred in the lee of the major volcanic peaks in the study area, as seen in the satellite imagery, including Fig. 10a. In the HRRR nest simulations wakes were also frequently present, as for example in the 12 November 2016 simulation shown in the supplemental material (Fig. ES1), and could extend hundreds of kilometers downwind. The WFIP2 dataset is rich with many other cases of mountain wakes, and research will be needed to document their impact on wind energy production. Because mountain wakes usually occur simultaneously with mountain waves, distinguishing their relative impacts will be challenging.

PHYSICS SITE, TURBINE WAKES, SURFACE ENERGY BALANCE. *Physics site.* The WFIP2 physics site was designed to measure the variability of key turbulence variables on spatial scales smaller than a current mesoscale model grid box. Observations from the physics site have only begun to be analyzed, and there is great potential to learn much from them. In Fig. 11, spatially averaged values of friction velocity $\langle u_* \rangle$ measured at 10-m height are compared to local estimates of u_* from the individual towers (listed in the legend) for the months of June and November 2016. The selected towers form both east–west and north–south transects through the physics site. Westerly winds dominated the site in June, with more frequent easterly winds in November.

Systematic differences are present in the turbulence variables measured during June 2016. Friction velocities are ~20% larger at P11 and ~24% smaller at P04 and P05, with no other significant differences found. Further investigations are underway to determine if these differences are due to topographic or surface roughness variations. In contrast, in November 2016, when the wheat crop was harvested and the winds were frequently out of the east, on average the spatial variability of friction velocity was much smaller. Also, in both months the surface heat flux was more spatially uniform than was the stress.

Turbine wakes in complex terrain. Scanning Doppler wind lidar measurements allow measurements of wind turbine wakes at multiple scales (Käsler et al. 2010; Banta et al. 2013; Aitken and Lundquist 2014; Iungo and Porté-Agel 2014; Banta et al. 2015). Although measurement of turbine wakes was not a central objective of WFIP2, two scanning lidars did provide observations useful for understanding wakes in complex terrain. Individual turbine wakes were observed in the lowest-elevation-angle conical scan of the lidar located at Arlington, which intersected the last-row wind turbines west of the instrument site (Fig. 12a). In addition, measurements of the wider-scale wind farm wake, suitable for comparison to mesoscale models (Fitch et al. 2012; Lee and Lundquist 2017; Redfern et al. 2018), can be obtained from the scanning lidar measurements as a function of downstream distance from the wind farm.

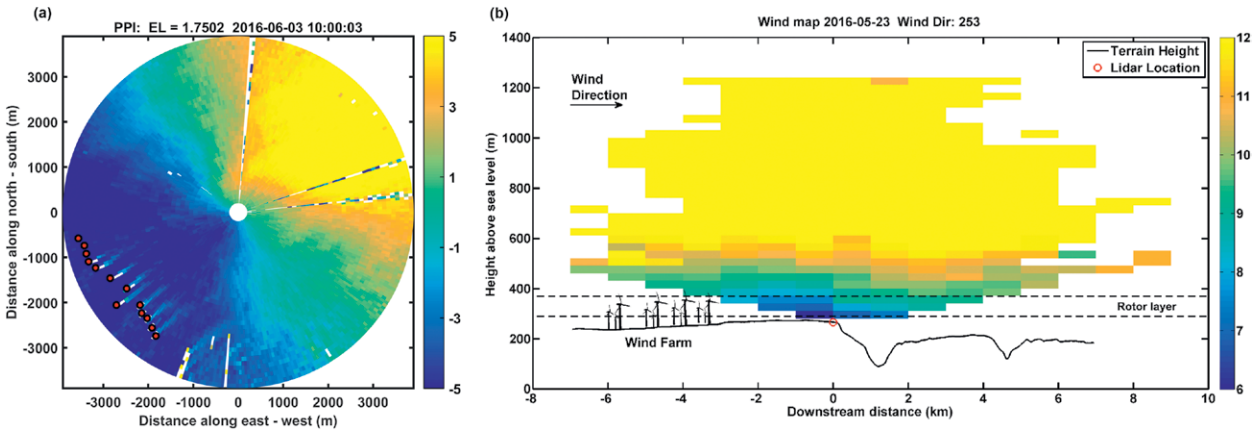

Fig. 12. (a) A low-elevation conical scan of radial wind speed from the Arlington lidar showing individual wind turbine wakes where individual turbine locations are indicated by the small red circles. (right) A two-dimensional cross section of the horizontal wind speed indicating the presence of a wind farm wake and its recovery farther downstream.

Figure 12b shows the downstream evolution of the wind field measured on 23 May 2016 from the scanning lidar at Arlington. Measurements from 1000 to 1200 UTC were composited together to smooth out the temporal variations and retain the average wake influence. The recovery of the wind farm wake can be clearly observed with downstream distance within the 200 m AGL layer (below 400 m ASL). In addition to the Arlington lidar, the scanning lidar at the physics site observed close-range wind turbine wakes over the physics site towers. Use of these measurements will enable investigation of wind plant wakes in complex terrain and how to account for them during model evaluation.

Surface energy balance observations. Surface energy exchange processes can have a large influence on meteorological phenomena important for wind energy production, and also can be important in determining the ability of NWP models to accurately forecast winds at turbine heights. Two surface-flux stations at the Boardman and Prineville sites included a full suite of turbulence, radiation, and soil observations required to measure all components of the surface energy budget. Wasco and the physics site included observations of momentum flux and sensible heat flux, and the latter site also included radiation and measurements of soil temperature and moisture as well as an energy balance Bowen ratio station. In addition, radiation measurements from the Rufus and Condon sites, as well as from Eugene, Oregon, allow for the characterization of spatial and seasonal variations of cloud amounts and downwelling shortwave, as shown in the supplemental material (Fig. ES2).

Figure 13 shows a 10-day average of the surface energy balance components at the physics site during August 2016 for both observed (solid lines) and 18-h-long HRRR retrospective control simulations that mimicked the NCEP HRRR configuration that was operational during WFIP2. During most daytime hours, the model shortwave down was too large, while the model shortwave and longwave up were too small, which in combination gave too much net radiative heating of the surface. The impact of this is seen in the sensible and latent heat fluxes, which were approximately 75 and 50 W m^{-2} too positive at solar noon, respectively. These results are consistent with those found at other WFIP2 sites and other time periods, and are due in part to inadequate treatment of subgrid-scale shallow cumulus, and surface albedo errors. Changes to the HRRR model to reduce these errors are discussed in the companion paper by Olson et al. (2019).

CONCLUSIONS AND OUTLOOK. The WFIP2 field program provides an extensive and detailed set of observations of flow in complex terrain. Networks of ground-based remote sensors (radar wind profilers, lidars, sodars and microwave radiometers) formed the core of the observing system, providing information over a range of spatial dimensions from the mesoscale down to model subgrid scales. The observations were collected in an area replete with a wide variety of terrain-influenced flows, including stagnant cold pools, gap flows, and mountain lee waves and wakes, as well as flows over more gently rolling terrain.

A principal purpose of collecting the WFIP2 observations was to improve model parameterizations,

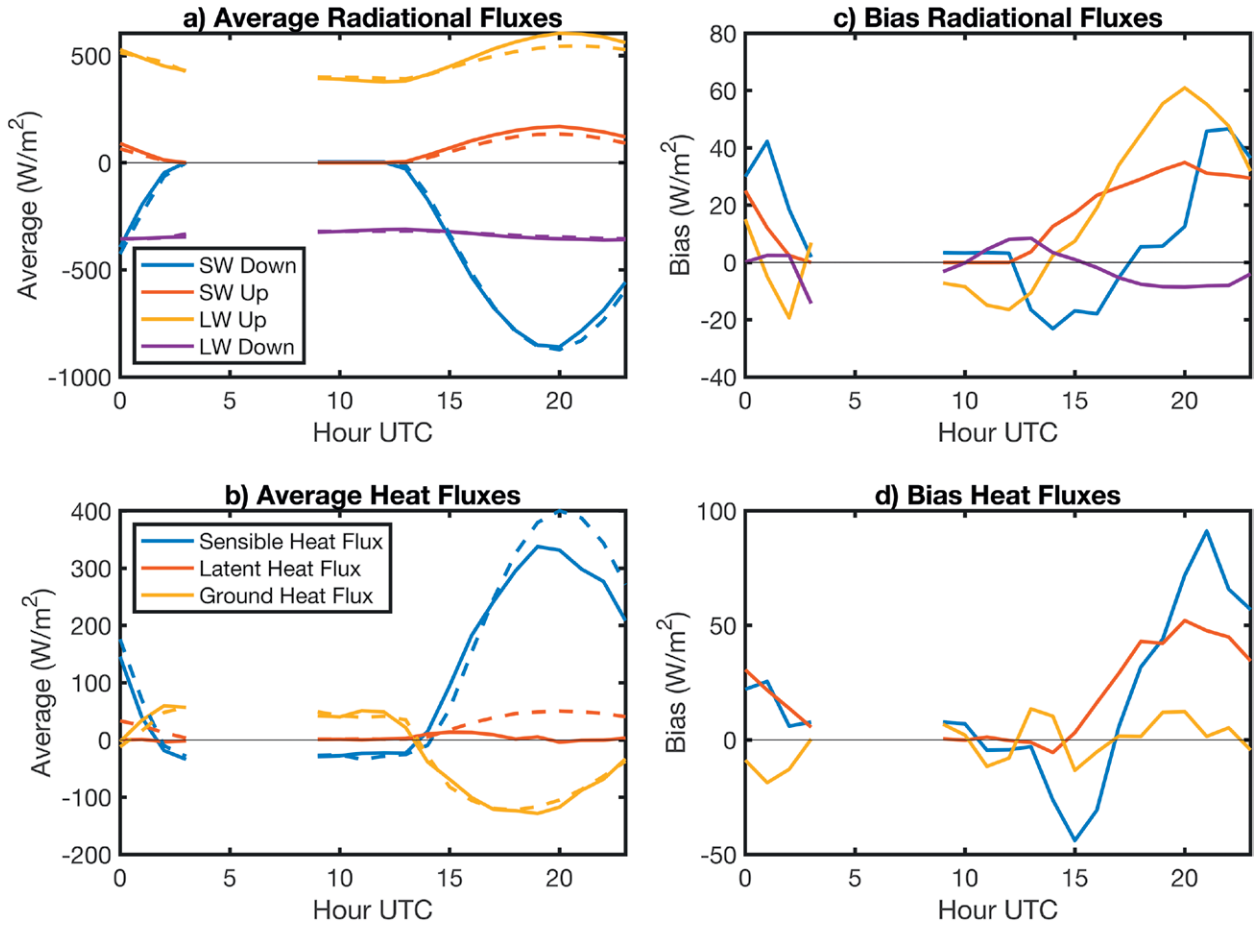

Fig. 13. Surface energy balance terms at the physics site averaged from 14 to 23 Aug 2016. (a) Four-component ratiative fluxes from observations (solid lines) and HRRR model (dashed lines). (b) Sensible, latent, and ground heat fluxes. (c) Radiation biases (positive values indicate excess surface heating). (d) Heat flux biases.

and the dataset has already led to significant improvements in the latest version of the NOAA operational HRRR model, not only in the Pacific Northwest, but across the entire United States (Olson et al. 2019). The current analysis has focused on using the observations to evaluate the skill of the version of the HRRR that was operational at the start of WFIP2, including identification of forecast busts, and to understand the physical processes associated with those model errors. The companion paper by Olson et al. (2019) describes using the observations to motivate and evaluate new parameterizations in model development case studies, iterating on the model changes until a satisfactory parameterization is achieved, and then evaluating the updated model over a longer set of simulations, demonstrating that the improvements were robust.

The WFIP2 program highlighted how challenging it is to materially improve model physical parameterizations. One aspect of the WFIP2 program that led to success in improving the HRRR model was the complementarity of the observations, measuring profiles of winds, temperature, and humidity, as well as radiation, surface fluxes, and soil properties at multiple supersite locations. The synergy of these observations allowed for key physical processes to be examined in detail and then contrasted to the model behavior. Having the capability to compare observations with model forecasts in real time facilitated advancements in our understanding of meteorological phenomena impacting wind energy, and helped develop ideas for potential model improvements. Finally, perhaps because of the complex terrain, it was essential to have a large number of spatially distributed sites measuring our key forecast improvement metric parameter, winds at turbine hub height (80 m), in order to develop statistically significant results. Evaluating the model at a small subset of the 22 verification sites could in many cases lead to erroneous conclusions about the full impact of the model changes.

Looking forward, many exciting research opportunities exist with the publically available datasets for anyone with interest, including investigations of the

accuracy of mountain wakes in models, the relation of surface pressure gradients and wind fields, the role of cloud and radiation errors on winds, and analyses of the surface energy budgets and surface model parameterizations. The WFIP2 observations have and will continue to provide new insights into the dominant meteorological phenomena in the region, and their impact on wind energy, and further model parameterization improvements will continue to be made using the WFIP2 observations.

ACKNOWLEDGMENTS. We thank the following individuals for help with some combination of site selection, leases, instrument deployment and maintenance, data collection, and data QC: Clark King, Jesse Leach, Tom Ayers, Daniel Wolfe, Timothy Coleman, Daniel Gottas, Scott Abbott, and Randy Nishiyama (NOAA/ESRL/PSD); Alan Brewer, Scott P. Sandberg, and Ann Weickmann (NOAA/ESRL/CSD); Clara St. Martin, Joseph Lee, Jessica Tomaszewski, and Joshua Aikins (CU-Boulder); Victor Morris, Mikhail Pekour, and Dan Nelson (DOE/PNNL); Jennifer Newman (formerly NREL), and Kevin Widener, G. Hodges, E. Hall, and J. Wendell. We also thank Billy Roberts (NREL) for drafting the physics site base map and Darren Jackson (NOAA) for processing GOES images. This work was authored (in part) by NREL, operated by the Alliance for Sustainable Energy, LLC, for the DOE, under Contract DE-AC36-08GO28308, with funding provided by the DOE Office of Energy Efficiency and Renewable Energy Wind Energy Technologies. Pacific Northwest National Laboratory is operated by Battelle Memorial Institute for the DOE under Contract DE-AC05-76RL01830. Lawrence Livermore National Laboratory is operated by Lawrence Livermore National Security, LLC, for the U.S. Department of Energy, National Nuclear Security Administration under Contract DE-AC52-07NA27344. NOAA was funded in part by DOE Grant DE-EE0007605. The views expressed in the article do not necessarily represent the views of the DOE or the U.S. government.

REFERENCES

Aitken, M. L., and J. K. Lundquist, 2014: Utility-scale wind turbine wake characterization using nacelle-based long-range scanning lidar. *J. Atmos. Oceanic Technol.*, **31**, 1529–1539, https://doi.org/10.1175/JTECH-D-13-00218.1.

Banta, R. M., Y. L. Pichugina, N. D. Kelley, R. M. Hardesty, and W. A. Brewer, 2013: Wind energy meteorology: Insight into wind properties in the turbine rotor layer of the atmosphere from high-resolution Doppler lidar. *Bull. Amer. Meteor. Soc.*, **94**, 883–902, https://doi.org/10.1175/BAMS-D-11-00057.1.

——, and Coauthors, 2015: 3D volumetric analysis of wind turbine wake properties in the atmosphere using high-resolution Doppler lidar. *J. Atmos. Oceanic Technol.*, **32**, 904–914, https://doi.org/10.1175/JTECH-D-14-00078.1.

Bianco, L., J. M. Wilczak, and A. B. White, 2008: Convective boundary layer depth estimation from wind profilers: Statistical comparison between an automated algorithm and expert estimations. *J. Atmos. Oceanic Technol.*, **25**, 1397–1413, https://doi.org/10.1175/2008JTECHA981.1.

Blackman, R., and J. Tukey, 1959: *The Measurement of Power Spectra*. Dover, 190 pp.

Bodini, N., J. K. Lundquist, and R. K. Newsom, 2018: Estimation of turbulence dissipation rate and its variability from sonic anemometer and wind Doppler lidar during the XPIA field campaign. *Atmos. Meas. Tech.*, **11**, 4291–4308, https://doi.org/10.5194/amt-11-4291-2018.

Bonin, T. A., and W. A. Brewer, 2017: Detection of range-folded returns in Doppler lidar observations. *IEEE Geosci. Remote Sens. Lett.*, **14**, 514–518, https://doi.org/10.1109/LGRS.2017.2652360.

——, and Coauthors, 2017: Evaluation of turbulence measurement techniques from a single Doppler lidar. *Atmos. Meas. Tech.*, **10**, 3021–3039, https://doi.org/10.5194/amt-10-3021-2017.

——, B. J. Carroll, R. M. Hardesty, W. A. Brewer, K. Hajny, O. E. Salmon, and P. B. Shepson, 2018: Doppler lidar observations of the mixing height in Indianapolis using an automated composite fuzzy logic approach. *J. Atmos. Oceanic Technol.*, **35**, 473–490, https://doi.org/10.1175/JTECH-D-17-0159.1.

Bougeault, P., and Coauthors, 1993: The atmospheric momentum budget over a major mountain range: First results of the PYREX field program. *Ann. Geophys.*, **11**, 395–418, https://hal.archives-ouvertes.fr/hal-01012319.

Durran, D. R., 1990: Mountain waves and downslope winds. *Atmospheric Processes over Complex Terrain*, *Meteor. Monogr.*, No. 23, Amer. Meteor. Soc., 59–81, https://doi.org/10.1007/978-1-935704-25-6_4.

——, 2003: Lee waves and mountain waves. *Encyclopedia of Atmospheric Sciences*, J. R. Holton, J. Pyle, and J. A. Curry, Eds., Elsevier, 1161–1169, https://doi.org/10.1016/B0-12-227090-8/00202-5.

Fitch, A. C., J. B. Olson, J. K. Lundquist, J. Dudhia, A. K. Gupta, J. Michalakes, and I. Barstad, 2012: Local and mesoscale impacts of wind farms as parameterized in a mesoscale NWP model. *Mon. Wea. Rev.*, **140**, 3017–3038, https://doi.org/10.1175/MWR-D-11-00352.1.

Frehlich, R., Y. Meillier, M. L. Jensen, B. Balsley, and R. Sharman, 2006: Measurements of boundary layer profiles in an urban environment. *J. Appl. Meteor. Climatol.*, **45**, 821–837, https://doi.org/10.1175/JAM2368.1.

Iungo, G. V., and F. Porté-Agel, 2014: Volumetric lidar scanning of wind turbine wakes under convective and neutral atmospheric stability regimes. *J. Atmos. Oceanic Technol.*, **31**, 2035–2048, https://doi.org/10.1175/JTECH-D-13-00252.1.

Käsler, Y., S. Rahm, R. Simmet, and M. Kühn, 2010: Wake measurements of a multi-MW wind turbine with coherent long-range pulsed Doppler wind lidar. *J. Atmos. Oceanic Technol.*, **27**, 1529–1532, https://doi.org/10.1175/2010JTECHA1483.1.

Krishnamurthy, R., R. Calhoun, B. Billings, and J. Doyle, 2011: Wind turbulence estimates in a valley by coherent Doppler lidar. *Meteor. Appl.*, **18**, 361–371, https://doi.org/10.1002/met.263.

Lee, J. C. Y., and J. K. Lundquist, 2017: Evaluation of the wind farm parameterization in the Weather Research and Forecasting Model (version 3.8.1) with meteorological and turbine power data. *Geosci. Model Dev.*, **10**, 4229–4244, https://doi.org/10.5194/gmd-10-4229-2017.

Marquis, M., J. Wilczak, M. Ahlstrom, J. Sharp, A. Stern, J. C. Smith, and S. Calvert, 2011: Forecasting the wind to reach significant penetration levels of wind energy. *Bull. Amer. Meteor. Soc.*, **92**, 1159–1171, https://doi.org/10.1175/2011BAMS3033.1.

Mass, C., D. Brees, and M. Albright, 1986: The onshore surge of marine air into the Pacific Northwest: A coastal region of complex terrain. *Mon. Wea. Rev.*, **114**, 2602–2627, https://doi.org/10.1175/1520-0493(1986)114<2602:TOSOMA>2.0.CO;2.

McCaffrey, K., L. Bianco, and J. M. Wilczak, 2017: Improved observations of turbulence dissipation rates from wind profiling radars. *Atmos. Meas. Tech.*, **10**, 2595–2611, https://doi.org/10.5194/amt-10-2595-2017.

Nance, L. B., and D. R. Durran, 1997: A modeling study of nonstationary trapped mountain lee waves. Part I: Mean-flow variability. *J. Atmos. Sci.*, **54**, 2275–2291, https://doi.org/10.1175/1520-0469(1997)054<2275:AMSONT>2.0.CO;2.

——, and ——, 1998: A modeling study of nonstationary trapped mountain lee waves. Part II: Nonlinearity. *J. Atmos. Sci.*, **55**, 1429–1445, https://doi.org/10.1175/1520-0469(1998)055<1429:AMSONT>2.0.CO;2.

Neiman, P. J., D. J. Gottas, and A. B. White, 2018: A real-time online data product that automatically detects easterly gap flow events and precipitation type in the Columbia River Gorge. *J. Atmos. Oceanic Technol.*, **35**, 2037–2052, https://doi.org/10.1175/JTECH-D-18-0088.1.

Olson, J. B., and Coauthors, 2019: Improving wind energy forecasting through numerical weather prediction model development. *Bull. Amer. Meteor. Soc.*, https://doi.org/10.1175/BAMS-D-18-0040.1, in press.

Piper, M., and J. K. Lundquist, 2004: Surface layer turbulence measurements during a frontal passage. *J. Atmos. Sci.*, **61**, 1768–1780, https://doi.org/10.1175/1520-0469(2004)061<1768:SLTMDA>2.0.CO;2.

Ralph, F. M., M. Crochet, and S. V. Venkateswaran, 1992: A study of mountain lee waves using clear-air radar. *Quart. J. Roy. Meteor. Soc.*, **118**, 597–627, https://doi.org/10.1002/qj.49711850602.

Redfern, S., J. B. Olson, J. K. Lundquist, and C. T. M. Clack, 2018: Incorporation of the rotor-equivalent wind speed into the Weather Research and Forecasting Model's wind farm parameterization. *Mon. Wea. Rev.*, **147**, 1029–1046, https://doi.org/10.1175/MWR-D-18-0194.1.

Reeves, H. D., and D. J. Stensrud, 2009: Synoptic-scale flow and valley cold pool evolution in the western United States. *Wea. Forecasting*, **24**, 1625–1643, https://doi.org/10.1175/2009WAF2222234.1.

Sharp, J., and C. Mass, 2002: Columbia Gorge gap flow: Insights from observational analysis and ultra-high-resolution simulation. *Bull. Amer. Meteor. Soc.*, **83**, 1757–1762, https://doi.org/10.1175/BAMS-83-12-1757.

——, and ——, 2004: Columbia Gorge gap winds: Their climatological influence and synoptic evolution. *Wea. Forecasting*, **19**, 970–992, https://doi.org/10.1175/826.1.

Shaw, W. J., and Coauthors 2019: The Second Wind Forecast Improvement Project (WFIP2): General overview. *Bull. Amer. Meteor. Soc.*, **100**, 1687–1699, https://doi.org/10.1175/BAMS-D-18-0036.1.

Smaliko, I. N., 2003: Techniques of wind vector estimation from data measured with a scanning coherent Doppler lidar. *J. Atmos. Oceanic Technol.*, **20**, 276–291. https://doi.org/10.1175/1520-0426(2003)020<0276:TOWVEF>2.0.CO;2.

Smith, R. B., J. Paegle, T. Clark, W. Cotton, G. Forbes, J. McGinley, H.-L. Pan, and M. Ralph, 1997a: Local and remote effects of mountains on weather: Research needs and opportunities. *Bull. Amer. Meteor. Soc.*, **78**, 877–892, https://doi.org/10.1175/1520-0477-78.5.853.

——, A. C. Gleason, P. A. Gluhosky, and V. Grubisic, 1997b: The wake of St. Vincent. *J. Atmos. Sci.*, **54**, 606–623, https://doi.org/10.1175/1520-0469(1997)054<0606:TWOSV>2.0.CO;2.

Smolarkiewicz, P. K., and R. Rotunno, 1989: Low Froude number flow past three-dimensional obstacles. Part

I: Baroclinically generated lee vortices. *J. Atmos. Sci.*, **46**, 1154–1164, https://doi.org/10.1175/1520-0469(1989)046<1154:LFNFPT>2.0.CO;2.

Welch, P., 1967: The use of the fast Fourier transform for the estimation of power spectra: A method based on time averaging over short, modified periodograms. *IEEE Trans. Audio Electroacoust.*, **15**, 70–73, https://doi.org/10.1109/TAU.1967.1161901.

Wells, H., S. B. Vosper, S. Webster, A. N. Ross, and A. R. Brown, 2008: The impact of mountain wakes on the drag exerted on downstream mountains. *Quart. J. Roy. Meteor. Soc.*, **134**, 677–687, https://doi.org/10.1002/qj.242.

Whiteman, C. D., S. Zhong, W. J. Shaw, J. M. Hubbe, X. Bian, and J. Mittelstadt, 2001: Cold pools in the Columbia basin. *Wea. Forecasting*, **16**, 432–447, https://doi.org/10.1175/1520-0434(2001)016<0432:CPITCB>2.0.CO;2.

Wilczak, J. M., and Coauthors, 2018: Data assimilation impact of in situ and remote sensing meteorological observations on wind power forecasts during the first Wind Forecast Improvement Project (WFIP). *Wind Energy*, **22**, 932–944, https://doi.org/10.1002/we.2332.

Zhong, S., C. D. Whiteman, X. Bian, W. J. Shaw, and J. M. Hubbe, 2001: Meteorological processes affecting the evolution of a wintertime cold air pool in the Columbia basin. *Mon. Wea. Rev.*, **129**, 2600–2613, https://doi.org/10.1175/1520-0493(2001)129<2600:MPATEO>2.0.CO;2.

JOIN US FOR THE CULMINATION OF OUR CENTENNIAL CELEBRATION

ATTEND THE 100TH AMS ANNUAL MEETING

12–16, JANUARY
BOSTON, MA

AMS100
AMERICAN METEOROLOGICAL SOCIETY
100TH ANNUAL MEETING | BOSTON | 2020

ANNUAL.AMETSOC.ORG